Università degli Studi di Napoli Federico II

Scuola Politecnica e delle Scienze di Base
Area Didattica di Scienze Matematiche Fisiche e Naturali

Dipartimento di Fisica "Ettore Pancini"

Corso di Laurea Magistrale in Fisica

Tracking hotspots around Sgr A*

Relatori
Prof. Mariafelicia De Laurentis

Prof. Alejandro Cruz-Osorio

Correlatore
Prof. Maurizio Paolillo

Candidato
Giuseppe Riveccio
N94000721

Anno Accademico 2022–2023

Università degli Studi di Napoli Federico II

Scuola Politecnica e delle Scienze di Base
Area Didattica di Scienze Matematiche Fisiche e Naturali

Dipartimento di Fisica "Ettore Pancini"

Corso di Laurea Magistrale in Fisica

Tracking hotspots around Sgr A*

Relatori
Prof. Mariafelicia De Laurentis

Prof. Alejandro Cruz-Osorio

Candidato
Giuseppe Riveccio
N94000721

Correlatore
Prof. Maurizio Paolillo

Anno Accademico 2022–2023

Abstract

Flares emitted by the supermassive black hole located at the center of our galaxy, Sagittarius A*, have been consistently monitored for decades across radio, NIR and X-ray wavelengths. Our knowledge about this phenomena is limited, nevertheless they could be explained by an hotspot orbiting close to the event horizon. Such object can be idendified as a plasmoid generated by magnetic reconnection. In this study, we employ ray traced imaging at 230GHz using the BHOSS code. We simulate a spherical region in circular orbit, where we modify the radiation coefficients. Additionally, we we investigate the influence of both thermal and non-thermal electron distributions within the model to account for the magnetic field responsible for plasmoid generation.

It is worth noting that our study is limited because we are not provided with observational data to compare our result aces limitations due to the absence of observational data for direct comparison. However, our results strongly suggest that such a hotspot should possess a radius of $2M$ and be situated at a distance of $6M$ from the black hole. Furthermore, the emission coefficient should be eight times greater than that of the background, taking into consideration the magnetic contribution to the electron distribution. This model presents a compelling explanation for the observed flare phenomena.

Contents

Introduction

Our Galaxy, The Milky Way

Observing the night sky on a clear, dark night, one can discern a prominent band stretching across the firmament. This celestial feature is none other than our own galaxy: the Milky Way. In the state of the art, it has a diameter of $26.8 \pm 1.1 kpc$(Goodwin, Gribbin, and Hendry 1998), a mass of $1.15 \times 10^{12} M_{\odot}$(Kafle et al. 2012) and it contains $1 - 4 \times 10^{11}$ stars(**MW_nstars**). For an extensive part of human history, the Milky Way was perceived as the entirety of the universe, and to this day, it remains one of the most scrutinized astrophysical entities. It wasn't until the 18th century that humanity began gaining a broader perspective on the cosmos, realizing that objects such as the Magellanic Clouds were distinct and separate from our galaxy. However, the transformative moment in our understanding occurred in the 1920s when Edwin Hubble revealed that the Milky Way is just one among countless galaxies. Specifically, it belongs to the category of barred spiral galaxies. As our observational capabilities advance, the Milky Way unfolds its mysteries, captivating our quest for knowledge. Of particular intrigue is the heart of our galaxy: the Galactic Center.

When we observe the Milky Way with the naked eye, the interstellar medium absorbs much of its emitted light. However, using telescopes equipped to detect infrared and radio waves reveals a luminous core at the galactic center. This becomes strikingly evident when examining Figure 1, which illustrates observations in different wavelength bands. At the top, we observe the galaxy in radio waves, while on the seventh and eighth place, there are near-infrared optical bands. The radiant region corresponds to the center of our galaxy, encompassing both its rotational and mass centers. It is widely accepted that a supermassive black hole resides at the core of nearly every galaxy, including our own. In our case, this entity is known as Sagittarius A* (Sgr A*).

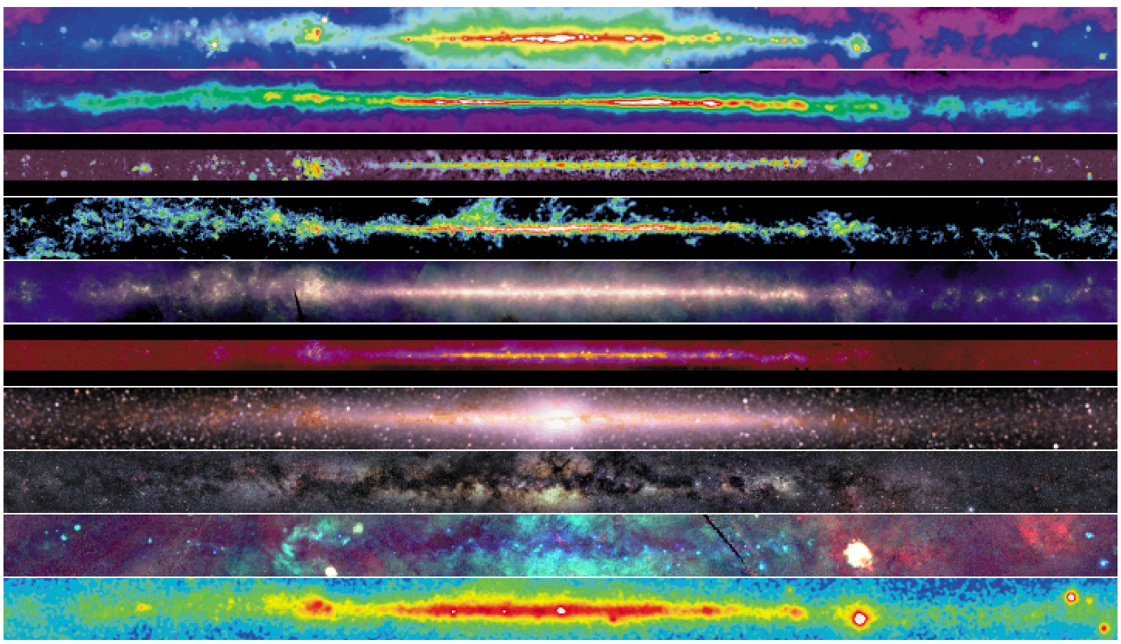

Figure 1: Image of the Milky Way in various wavelengths of light from top to bottom as follows: radio at 408 MHz, atomic hydrogen 1.4 GHz, radio ind the range 2.4-2.7 GHz, molecular hydrogen 115 GHz, composite mid and far infrared in $3 - 25 \times 10^3$ GHz, mid infrared in the same range as the previous, near infrared (NIR) in $86 - 240 \times 10^3$ GHz, optical 460×10^3 GHz, x-ray in $60 - 360 \times 10^6$ GHz, and gamma-ray $> 2.4 \times 10^{13}$ GHz. These illustrates how different features are more prominent in different flavors of light. Credit NASA.

Evidence for a Black Hole at the galactic center

The center of our galaxy has interested many groups of scientist throughout the century observing, it was first observed as a radio source in 1933 by Karl Jansky. However, it wasn't until the 1980s that this mysterious object was conclusively identified as a supermassive black hole at the heart of our galaxy (see Genzel, Hollenbach, and Townes 1994). At that time, its mass was estimated to be approximately 3 million times that of the Sun. This estimation was grounded in the observation of stars within close proximity exhibiting increased velocities, a strong indicator of a massive compact object, such as a black hole. Significant advancements in measuring the mass of Sagittarius A* (Sgr A*) occurred when scientists closely analyzed the motion of stars orbiting around it, aptly named the S-stars. Specifically, it was studied the motion of the star S2 throughout its whole orbit (with an estimated period of $\sim 15yrs$), measuring the near infrared emission due to the reduced interstellar exintion. In 2002, it was reported that Sgr A* had a mass of $M = (4.1 \pm 0.6) \times 10^6 M_\odot$(Ghez et al. 2003) and in 2022 the precision has been increased $M = (4.297 \pm 0.012)10^6 M_\odot$ (GRAVITY Collaboration, Abuter, R., et al. 2023). Yet, the resolution needed to detect directly the central compact object (around dozens of μas) was beyond the available; in order to comply with this issue, it is needed a telescope with the same diameter as the Earth. Furthermore the bolometric luminosity produced by the surrounding gas is $< 100 \times 10^{36} \frac{erg}{s}$ ($\sim$ 100 time the Sun luminosity), meaning that if situated in an other galaxy, it would go easily undetected. Direct imaging of this compact object remained elusive until the historic release of an image by the Event Horizon Telescope collaboration (EHT) in 2022 (refer to EHT 2022a, and fig. 2), here it is shown the result of 5 night of observation, the final image is obtained averaging between various reconstruction method. This monumental achievement provided unequivocal visual evidence of the existence of the compact object predicted by theoretical models over a century ago (the more general Schwarzshild black hole model). Importantly, it's worth noting that the image of Sgr A* in 2022 was not the first image of a black hole. In 2019, the same collaboration (EHT) made headlines by capturing an image of the black hole in M87, situated at the center of the Virgo A elliptic galaxy (often called M87[1]) in the Virgo clusterEHT et al. 2019. The mass of Sgr A* was reconstructed through relativistic calculations based on the shadow of the black hole, which is the effective representation observed through telescopes due to the bending of light. These calculations confirmed the previous mass estimates, yielding a value of approximately $\sim 4 \times 10^6 M_\odot$. The first simulated image of a black hole was provided by Luminet 1979 and it is shown in fig.**??**. To infer the black hole parameters from the observation, they performed numerical

[1]The name M87 identifies both the supermassive black hole and the specific galaxy, the latter represents the main member of the Virgo cluster where it is situated. The cluster itself is the most massive component of the Virgo super-cluster.

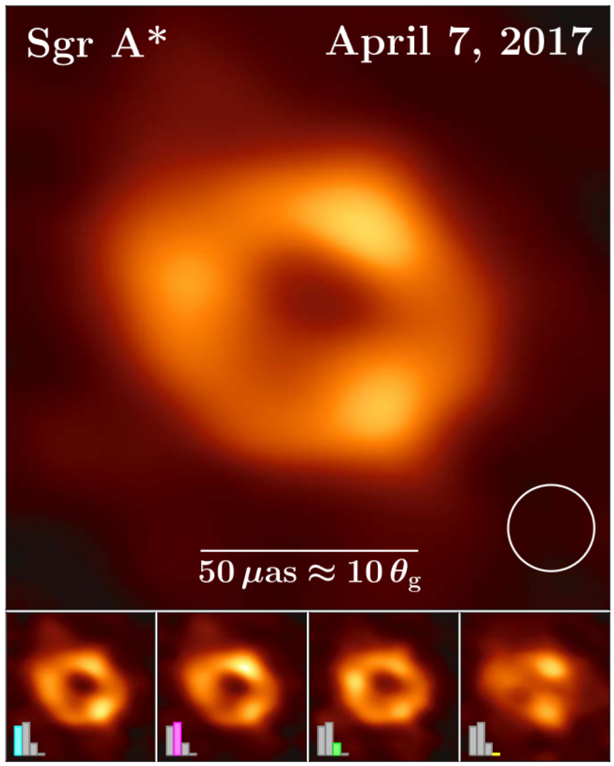

Figure 2: Black hole shadow and emission at 230 GHz EHT 2022a. The top images is an average over various subsets taking the inserted white circle as a reference beam for the reconstruction process. On the bottom, there are the averages taking similar morphologies and their relative abundance inside the subsets. The color scale represents the specific intensity in terms of temperature.

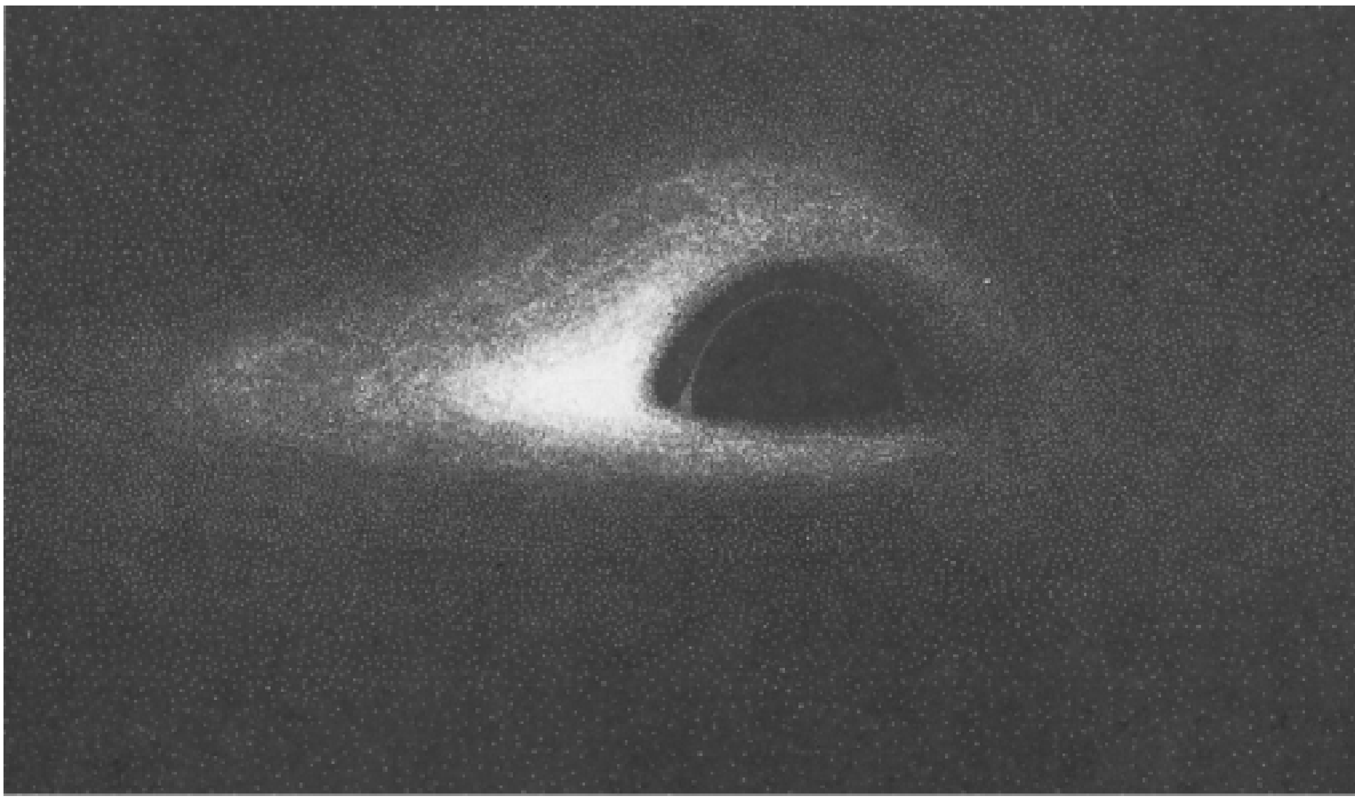

Figure 3: First simulated image of a spherical black hole with thin accretion disk. The system is seen from a great distance by an observer at 10° above the disk's plane.

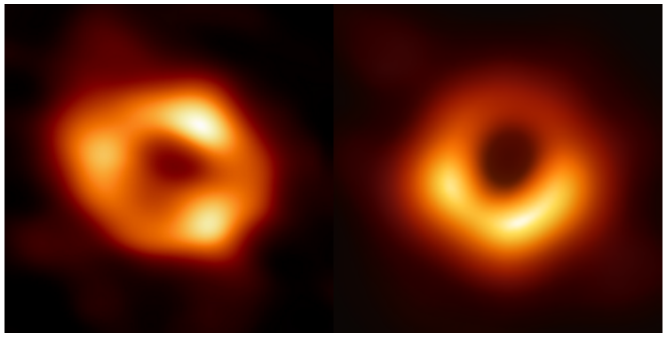

Figure 4: On the left the observation of Sgr A* from EHT 2022a, on the right M87 from EHT et al. 2019.

simulations (see EHT 2022b) and concluded that Sgr A* is most likely a Kerr black hole with strongly magnetized gas (MAD, magnetically arrested disk) which creates a jet. In this scenario, the system should have inclination of $i = 30$ respect to the plane of the sky and spin parameter $a = 0.5$ (see section 1.3 for details). These simulations do not explain all the possible behaviour[2] but represent a first approximation that allow for further investigations. We will go through all the mathematical details in the next chapter. This breakthrough opens up to whole new possibilities to understand the physics around such compact objects; if we have a look to fig. 4 we can see the observation of Sgr A* on the left and M87 on the right. The image obtained previously of M87 in EHT et al. 2019 showed smooth emission region, while for our protagonist it is immediate to notice the presence of 3 regions more luminous than the rest. The issue is thought to be related to the phenomena of flares and the presence of a "hotspot".

Evidence for Sagittarius A* flares

Sagittarius A* was first known as a radio source and, in the second half of the century, scientists began to see unexpected events. In 1980s it was detected, by Brown and Lo 1982, a variation of the lightcurve at $2695MHz$ between 25% and 40% of over a few days.

Around the beginning of the 2000s, many measured simultaneous signals in various wavebands (see Falcke et al. 1998, An et al. 2005, Eckart et al. 2006). Likewise, Falcke et al. 1998 presented detections over two days ranging from radio to infrared; they found the total flux of the source to be $(2.9 \pm 0.25)Jy$ at 152.3 GHz, although the value at this wavelength expected by their fit should have been $\sim 2Jy$, this may be due to its variability. On the other side, detections of the variability were found also in X-ray (as in Baganoff

[2] It is not to our knowledge whether the theory of General Relativity holds in very strong field like in the vicinity of a black hole event horizon, nevertheless all the numerical simulation are processed in this framework. It is evident that the results, shown in EHT 2022b, do not replicate the morphology in fig.2.

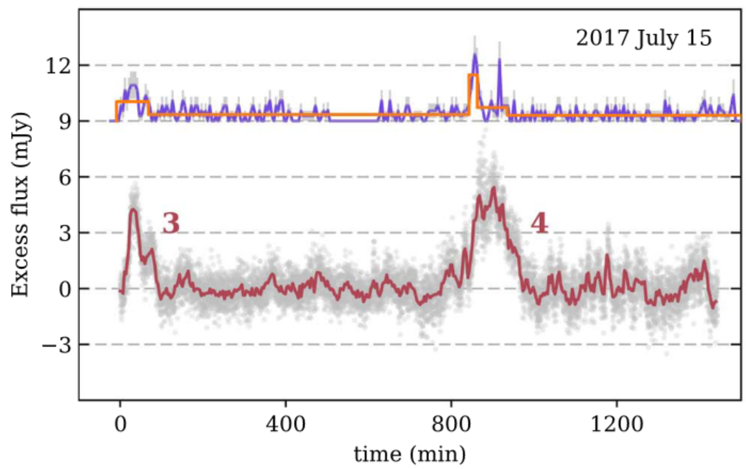

Figure 5: Simultaneous IR and X-ray light curves of Sgr A* (Boyce et al. 2019). Plotted in gray/red is the excess flux density (mJy) of the pixel containing Sgr A* from Spitzer $4.5\mu m$. Chandra light curves of Sgr A* at 2–8 keV are plotted in purple with an offset inserted. The orange line represent the most probable value to measure through the a specific time interval The peaks are respectively the third and the fourth event observed during the whole Chandra observation (meaning in x-ray).

et al. 2003), with a timescale about thousands of seconds. Only in 2019 it was confirmed whether the events in infrared and X-ray could be considered simultaneous[3](see Boyce et al. 2019), this implies that the flares are physically connected.This that the events could be actually caused from the same physical phenomena.

As shown in Maciek Wielgus et al. 2022 and in Chen et al. 2019, in the last 20 years we have been constantly collecting datas on these flares, showing similar impulsive spectrum also for millimiters wavelengths (Marrone et al. 2008, Eckart et al. 2006). A measurement showed a total flux of the order of $2-4Jy$ and a variation $\sim 1Jy$ at 230GHz, while similar behaviour was found for more energetic bands but on the order of mJy. After analyzing the also the polarization, (see Marrone et al. 2008,Dodds-Eden et al. 2009,Ponti et al. 2017) it was confirmed that the emission is best fitted by to synchrotron emission with high power law tail and engaged with a cooling mechanism (see Yuan, Quataert, and Narayan 2004,Yusef-Zadeh et al. 2006,Boyce et al. 2019, Dodds-Eden et al. 2009), this comes from the already known cooling synchrotron system, meaning that with the radiation emission the gas looses energy implying a net decrease of temperature. In fig. **??** is shown a representative flare extracted from Boyce et al. 2019. It is evident how the two flares presented visibly excess the noise both in x-ray and IR.

[3]The study takes count of multiple flares measured in infrared and x-ray respectively by Spitzer and Chandra telescopes. The difference between the peaks of emission was always found to be around 10 minutes. Nevertheless, taking into account a 3σ interval, the flare can be considered simultaneous.

Flares have been continuously measured over decades (Chen et al. 2019) but still there is no evidence for a suitable explanation on how they are generated. Nowadays most of the the dominant view is that the behaviour is caused by an hotspot. We will discuss more about this topic in the next section.

Evidence for a hotspot

The most explored line of research is an object star-like orbiting around the black hole, a hotspot. This would explain the strong flares, they could be due to relativistic effect of gravitational lensing when the hotspot passes behind the compact object. Furthermore, the type of emission is synchrotron, meaning that the hotspot is submerged in a strong magnetic field and this could explain also how it could be created (see Aimar et al. 2023): a plasmoid generated by magnetic reconnection. Such plasmoid can be thought as a magnetic trap for the plasma that heats the particles inside, it can have various shape its emission properties will depend on the gas and the magnetic field that generated it, but an important contribution comes from the surroundings since the radiation will be transported; moreover it can have various shapes like a torus or a star-fish (see Bostick 1957), although for astrophysical purposes the spherical shape it's reasonable, see Aimar et al. 2023)

Already 20 years ago, in Broderick and Loeb 2005, there were numerical simulations on how it could appear such plasmoid around a black hole, it is indeed similar to what has been developed for this thesis. Definitive reason to investigate the hotspot may come from the following:

- In M. Wielgus et al. 2022 it is studied the polarization by ALMA at 229 GHz, they compared it with a simulation having a spherical object at a finite temperature orbiting around a black hole on the equatorial plane. It was found polatimetric loops in the Q-U plane[4]. Their best model is an hotspot of $\sim 3r_g$ radii at $11r_g$ distance in clockwise rotation with an inclination angle of $i \leq 30°$.

- In 2020 GRAVITY collaboration published a study on the motion of the centroid of these flares (see GRAVITY Collaboration, Bauböck, M., et al. 2020). They analyzed 3 events in 2017, so they computed the best fit for a circular orbit in a Kerr-Newmann space-time (a charged rotating black hole). The conclusion was that the orbit have to around 8M and 10M of distance from the center of the black hole with inclination angle $120 < i < 150$, this also means clockwise rotation.

[4]The polarization can be identified with the Stokes indexes: I, Q, U, V. The first represents the total intensity, the second and third are the linear polarization + and x, the last is the circular polarization. For details see Jackson 1998.

- In Aimar et al. 2023 is studied the production and the behaviour of a plasmoid by magnetic reconnection using resistive GRMHD. They conclude that having viscous systems is the only way to produce such an object, this can be created very close to the ergosphere, it can have a radii of $1-3r_g$ situated at $5-10r_g$ from the black hole (at the point where it stays in orbit).

Since the main candidate to represent the hotspot is the plasmoid, we will use also a non-thermal electron distribution function to better simulate the strong interaction that may lead to the plasmoid production. These results are consistent with each other and combining them we come up with our toy model. We will simulate the presence of a spherical region orbiting the black hole for ray tracing. This object will be in circular orbit on the equatorial plane. We will study different values for emissivity and absortivity of the gas inside, this way we do not change by hand the datas from the GRMHD simulation, on the opposite we assigning a different physical property of the gas locally. This toy model allow us to simulate trivially the interaction of the plasmoid with the surrounding gas.

Going through the thesis the reader will learn the essentials about black holes and the motion around them (chapter 1), then it will be necessary to learn how the electron behave to generate emission in a thermal and non-thermal models and how this emission should be transported out into the empty space (chapter 2). After the theoretical background we will learn about the toy model, proposed in this thesis, and the workflow that has been carried out (chapter 3) and we will show the results (chapter 4) with conclusions (chapter 5) at the end. This thesis contains the theory essential of what the reader needs to understand the project here presented. For whoever is particularly interested in some topics I may suggest some books/paper I used: black holes Chandrasekhar 1992(detailed) O'Neill 1995(more on the meaning of things) Rezzolla and Zanotti 2013 (essential), gas structure around the black hole Rezzolla and Zanotti 2013 (detailed)Abramowicz and Fragile 2013 (generally good to stard with), non-thermal distribution Marian Lazar and Fichtner 2021 Livadiotis and McComas 2009(extensive and detailed for my purpose).

–1–
Black hole physics

Contents: **1.1 Pills of General Relativity. 1.2 How we define a black hole. 1.3 Kerr geometry. 1.4 Geodesic motion. 1.5 Geodesic motion for ray tracing. 1.6 Gas around a black hole.**

The black hole is one of the most intriguing astrophysical object ever discovered, it represents a region where the gravitational pressure it is so high that all the matter collapses into a single point. Gravity can become so strong that, closer than a certain distance, it is impossible to come back, even for light. We call this limit the event horizon, this name stands because of the impossibility of observing events that happen beyond it. In the following sections, we will get an idea of the building blocks of the theory and the simplest black hole case (section 1.2), how to describe a rotating one (section 1.3), how the particles move around it and how light travels before reaching our telescopes (section 1.4). We observe the black hole through electromagnetic radiation, so we need to understand about its radiation transport through the matter (section 2.1) and about the emission and absorption properties (section 2.2).

1.1 Pills of General Relativity

The theory of General Relativity proposed by A. Einstein is a cornerstone of modern scientific thought (see the original paper in Einstein 1915). It has revolutionized our understanding of gravity and space-time, it has led to many important consequences in physics and astronomy. One of its most famous discoveries is the black hole solution, which has fascinated scientists and the public alike for decades. Understanding the complexities of this theory is crucial for advancing our scientific knowledge and exploring the mysteries of the universe. We will not go through all the details of the theory but just the essential parts for our aim, for more see Misner, Thorne, and Wheeler 1973.

The theory is based on the idea that we live in a 4-dimensional space called manifold, this identifies what is commonly known as space-time. Such manifold can be imagined as a surface that can bend and change shape arbitrarily. We will choose a particular shape and symmetry to build our space-time (suitable to our problem) and when we talk about a specific one, we refer to a solution to the Einstein field equations, as follows:

$$G_{\mu\nu} = \chi T_{\mu\nu}. \tag{1.1}$$

On the left of this equation, there is the Einstein tensor $G_{\mu\nu}$ which represents the geometrical contribution of the manifold, while on the other side, there is the constant[1] $\chi = \frac{8\pi G}{c^4}$ and the energy tensor $T_{\mu\nu}$ that gives the contribution of the matter laying inside the space-time. As J. Wheeler said, space-time tells matter how to move, matter tells space-time how to curve (Misner, Thorne, and Wheeler 1973, Carroll 2019). The Greek indexes μ and ν can vary from 0 to 3, where 0 stands for the time component while all the other represents the space components. This index system is utilized for describing all tensors and vectors in space-time, including the position x^μ and velocity u^μ (for more see Misner, Thorne, and Wheeler 1973,). The way to formalize the shape of a space-time is to describe how the distance is measured. In particular, we are interested in the infinitesimal distance inside this 4-dimensional manifold defined as follows

$$ds^2 = g_{\mu\nu} dx^\mu dx^\nu. \tag{1.2}$$

To solve the Einstein equations means finding the metric tensor $g_{\mu\nu}$ in the formula just shown and, once we know its shape, we can possibly tell everything about our space-time. When using the diagonal form of a metric, the components have to be three of the same sign and one of the opposite, and in this thesis, we will use the convention (-,+,+,+); this describes a pseudo-Riemaniann manifold. These instruments are used to build space-times with various shapes and properties and here, as one could expect, we are interested in the black hole solution that we are going to explain briefly in the next section. To numerically simulate the spacetime we need to implement the ADM 3+1 formalism. It consists to foliate the spacetime in space hypersurface identified by the time coordinate, in this framework the spacetime is described as follows:

$$ds^2 = -(\alpha^2 - \beta_i \beta^i) dt^2 + 22\beta_i dx^i dt + \gamma_{ij} dx^i dx^j, \tag{1.3}$$

where α is the lapse function, β^i is the shift vector and γ_{ij} is the spatial metric of the

[1]The theory of General Relativity improves the knowledge about gravity, nevertheless in the weak field regime (also called Newtonian limit) it has to match the results from the classical mechanics. This requirement allow to determinate this formulation of the constant χ (the Einstein equation for $\mu = 0$ and $\nu = 0$ matches the Poisson's equation for the gravitational potential $\nabla^2\Phi = 4\pi G\Phi$).

foliation (Rezzolla and Zanotti 2013).

1.2 How we define a black hole

In 1916, Karl Schwarzschild found the first exact solution of Einstein's equations in vacuum (see Schwarzschild 1916). It describes a stationary, static and spherically symmetric space-time, where all the mass is concentrated in one point taken as the origin of our coordinate system; this generates a singularity[2]. This black hole is defined only by its mass, which can be measured by observing its event horizon dimensions. The latter is defined a spherical surface of radius $R_S = \frac{2GM}{c^2}$(called Schwarzschild radius) that surrounds the singularity. Signals cannot exit this surface, meaning that we are not able to have information about the region inside the event horizon, therefore its name.

To describe formally this space-time, we have to define the distance between the points, so the line element is

$$ds^2 = -\left(1 - \frac{R_S}{r}\right) dt^2 + \left(1 - \frac{R_S}{r}\right)^{-1} dr^2 + r^2 d\Omega^2, \tag{1.4}$$

where Ω represents the solid angle, while t is the time coordinate and r is the radial coordinate. Notice the signs (-,+,+,+) as the convention we are using. In this solution, as r approaches R_S, the first coefficient (g_{tt}) goes to zero, while the second coefficient (g_{rr}) diverges. This means that on the event horizon the space-time is infinitely "stretched"[3] and, as a result, all signals will be affected becoming non-measurable: they will have infinite wavelength (or null frequency). We refer to this effect as infinite redshift (see Rezzolla and Zanotti 2013).

This is the most basic form of black hole space-time. However, a more complex and real scenario involves rotation. In the following section, we will explore rotating black holes.

1.3 Kerr geometry

The Schwarzshild solution have been useful for many reasons: it was the first solution ever of the theory, it was used to infer for the first time the gravitational lensing and to solve the famous problem of precession at the perielia of Mercury(see Misner, Thorne,

[2]By singularity, we mean a divergence of some quantity. We can distinguish the coordinate singularity, which can be avoided with a coordinate transformation, and the physical singularity, which is intrinsic of the space-time. In this particular case, we were referring to a physical singularity.

[3]This is from the point of view of a distant observer, like us from the Earth. Nevertheless nothing really happens to any object passing through the event horizon. This represents a coordinate singularity, meaning that it can be avoided adopting a trasformation (e.g. using Kruskal–Szekeres coordinate system).

and Wheeler 1973). Still, it represents an approximation: spherical symmetry do not allow the object to have angular momentum but almost all astrophysical systems have angular momentum in general. Nevertheless it is reasonable to think that a system with such rotation will generate a black hole with the same property. The solution of describing such objects was first found almost fifty years later the non-rotating case by Roy Kerr in 1963 (for more details, see Chandrasekhar 1992 and Abramowicz and Fragile 2013).

In order to solve the field equation we need to reduce the degrees of freedom; this is because, up to now, a general solution is yet to be found. We expect that the space-time of a rotating black hole should have axial symmetry, it should also be stationary to assure the conservation over time; to obtain so, we require these properties from the general line element (eq. 1.2) imposing e.g. the metric coefficient should be a function of only the distance r and the polar angle θ as $g_{\mu\nu}(r,\theta)$. The full derivation formulation is not our aim but the interested reader can have a look to Chandrasekhar 1992 for details. The line element is

$$ds^2 = -\left(1 - \frac{2Mr}{\rho^2}\right) dt^2 - \frac{2Mar}{\rho^2} sin^2\theta \, dt \, d\phi + \frac{\rho^2}{\Delta} dr^2 + \rho^2 d\theta^2 + \frac{\Sigma}{\rho^2} sin^2\theta \, d\phi^2, \tag{1.5}$$

where

$$\begin{aligned} \Delta &:= r^2 - 2Mr + a^2, \qquad \Sigma := (r^2 + a^2)^2 - a^2 \Delta sin^2\theta, \\ \rho^2 &:= r^2 + a^2 cos^2\theta, \qquad a = \frac{J}{M}. \end{aligned} \tag{1.6}$$

Here we used the spherical set of coordinate called Boyer-Lindquist, moreover from here on we will take $c = G = 1$. The quantity that identifies the mass is M, while the angular momentum will be represented by J; these are used to define spin parameter $a = \frac{J}{M}$. When $a = 0$ it leads to the Schwarzshild geometry, while the case $a = M$ is referred as the maximally rotating black hole. Here we can distinguish the surface for infinite redshift and event horizons, they are respectively determined by imposing $g_{tt} = 0$ and $g_{rr} \to \infty$ (to recall the meaning, we say infinite redshift when a signal coming to this region will be infinetly stretched becoming unmeasurable, while event horizon is the region where no signal can escape to infinite distance). These surfaces merge together as we recover the non-rotating case $a = 0$. This being said, the condition for infinite redshift yields

$$r_{z\pm} = M \pm \sqrt{M^2 - a^2 cos^2\theta}, \tag{1.7}$$

and the other for the event horizon is

$$r_{h\pm} = M \pm \sqrt{M^2 - a^2}. \tag{1.8}$$

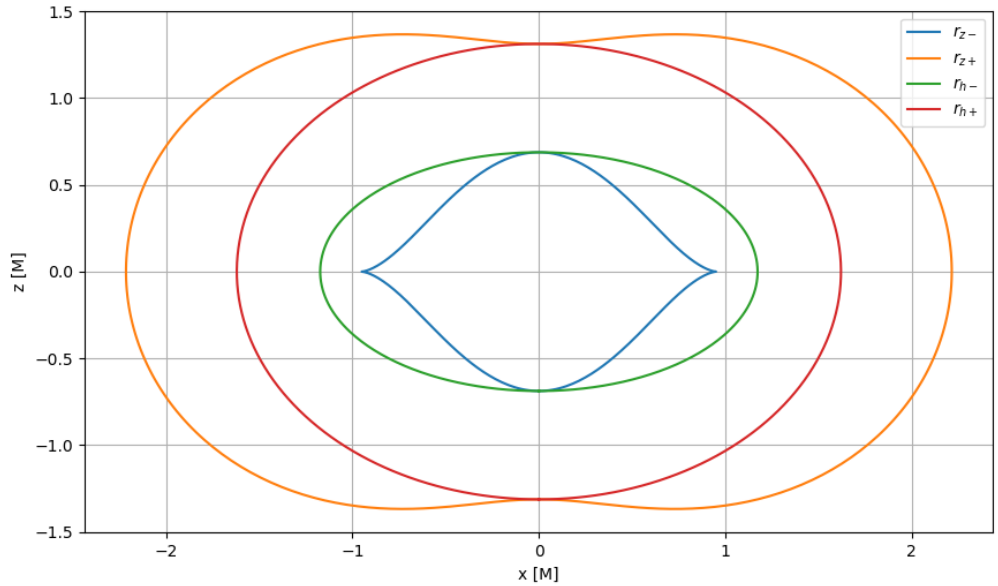

Figure 1.1: Representation on the x-z plane with $a = 0.95$ and $M = 1$of the internal ergosphere r_{z-} (in blue), the external ergosphere r_{z+} (in orange), the internal event horizon r_{h-} (in green) and the external event horizon r_{h+} in red. In the x-y plane it would be, in the same order, just concentric circles due to axis symmetry.

In this geometry there is a purely relativistic effect called frame dragging: the black hole rotation warps the space-time so that any particle will be pushed to co-rotate. There is a region where the effect is so strong that even photons are forced to rotate and no static observer can exist, this is called ergoregion and it is situated inside r_{z+} that defines the ergosphere. It is straight forward to see that for $a = 0$ the horizons converge to R_S, for $a = M$ they will both approach $r_{h\pm} = M = R_S/2$.The existence of the ergoregion can be demonstrated by using the ZAMO approach (Zero Angular Momentum Observer, for more details see Abramowicz and Fragile 2013). This is done taking the angular momentum, eq. 1.16, to be always zero, this implies that inside the ergosphere such observer will become superluminal (meaning that its speed should be greater than light speed). A representation of these surfaces it is shown in fig. 1.1. In the case $|a| > M$ we will not see the event horizons and this will be called a naked singularity, so the existence of an horizon forces the spin parameter to be $|a| < M$. Moreover we can define the innermost stable circular orbit (ISCO) as follows

$$r_{\text{ISCO}} = \frac{GM}{c^2}\{3 + Z_2 - [(3 - Z_1)(3 + Z_1 + 2Z_2)]^{\frac{1}{2}}\}, \tag{1.9}$$

where $Z_1 = 1 + \left(1 - a_*^2\right)^{1/3} \left[\left(1 + a_*\right)^{1/3} + \left(1 + a_*\right)^{1/3}\right]$, $Z_2 = \left(3a_*^2 + Z_1^2\right)^{1/2}$ and $a_* = \frac{a}{M}$. The fig. 1.1 has been evaluated through a change of coordinate from B-L to cartesian, formally as follows:

$$\begin{aligned} x &= \sqrt{r^2 + a^2}\, \sin\theta \cos\phi, \\ y &= \sqrt{r^2 + a^2}\, \sin\theta \sin\phi, \\ z &= r\cos\theta. \end{aligned} \tag{1.10}$$

Kerr-Schild formulation

For numerical purposes it is more convenient to use other sets of coordinates like Kerr-Schild coordinates which avoid coordinate singularities, for more details see Chandrasekhar 1992 or Rezzolla and Zanotti 2013. The divergences can be "cured" by defining

$$dt' = dt + \frac{2Mr}{\Delta} dr, \qquad d\phi' = d\phi + \frac{a}{\Delta} dr. \tag{1.11}$$

This way the line element becomes

$$\begin{aligned} ds^2 = &- (1 - B) dt'^2 - 2Ba\, sin^2\theta\, dt'\, d\phi' + 2B\, dt'\, dr - 2a(1 + B) sin^2\theta\, dr\, d\phi' + \\ &+ (1 + B)\, dr^2 + \rho^2 d\theta^2 + \frac{A\, sin^2\theta}{\rho^2}\, d\phi'^2, \end{aligned} \tag{1.12}$$

where $B := \frac{2Mr}{\rho^2}$. The only physical singularity in both sets of coordinates it is a physical one yielded by $\rho = 0$, which means $r = 0$ and $\theta = \frac{\pi}{2}$, so it will be a ring-singularity.

Now that we have an idea on how this space-time is shaped, we have to analyze how the particles move inside it. We want to study the geodesic motion.

1.4 Geodesic motion

We recall that we want to simulate an object orbiting a black hole, here we want to understand how a free particle should move in such manifold. The motion is subjected only to the curvature of the space-time, hence the gravity; it is called geodesic motion.

In this geometry, the motion is defined by conserved quantities: the angular momentum L, the energy E and the Carter constant Q but we will need only the first two; it is not the aim here to analyze the details of a general motion and its property but only a stable one in the equatorial plane.

Equatorial motion

A way to easily infer the equations of motion is to minimize the line element over the proper time, this means applying the Euler-Lagrange equations[4]. A general way to write the Lagrangian is simply

$$\mathcal{L} = \frac{1}{2} g_{\mu\nu} \frac{dx^\mu}{d\tau}\frac{dx^\nu}{d\tau}, \tag{1.13}$$

which we remember to be the derivative of the line element respect to the affine parameter. The latter is on directly the curve, moreover τ is generally known as the proper time. The latter represents the time in the coordinate system solidal to the particle in motion, in this system the particle is not moving so $ds^2 = g_{00}dt^2 = d\tau^2$. In our case the motion is planar so we take $\theta = \frac{\pi}{2}$ and $\dot{\theta} = 0$, it follows

$$2\mathscr{L} = \left(1 - \frac{2M}{r}\right)\dot{t}^2 + \frac{4aM}{r}\dot{t}\dot{\phi} - \frac{r^2}{\Delta}\dot{r}^2 - \left[\left(r^2 + a^2\right) + \frac{2a^2M}{r}\right]\dot{\phi}^2. \tag{1.14}$$

If we apply the equations in ϕ and t we can find the constant of motion associated with the axial symmetry and stationary requirement, explicitly their momenta are

$$p_t = \left(1 - \frac{2M}{r}\dot{t} + \frac{2aM}{r}\dot{\phi}\right) = E = constant, \tag{1.15}$$

$$p_\phi = \frac{2aM}{r}\dot{t} - \left[\left(r^2 + a^2\right) + \frac{2a^2M}{r}\right]\dot{\phi} = L = constant. \tag{1.16}$$

On the other hand the momenta in radial direction is not constant, as follows

$$p_r = -\frac{r^2}{\Delta}\dot{r}. \tag{1.17}$$

The Carter constant is missing because it is null for the equatorial motion, as follows

$$Q = p_\theta^2 + \cos^2\theta\left[a^2\left(m^2 - E^2\right) + \left(\frac{L_\phi}{\sin\theta}\right)^2\right] = 0, \tag{1.18}$$

[4]In classical Newtonian mechanics, these equation are equivalent to the second law of dynamics. In general relativity they are equivalent to the geodesic equation 2.14. Here there are respectively the equations and the generalized momenta:

$$\frac{\partial\mathcal{L}}{\partial x^\nu} = \frac{d}{d\tau}\left(\frac{\partial\mathcal{L}}{\partial\dot{x}^\nu}\right), \qquad p_\nu = \frac{\partial\mathcal{L}}{\partial\dot{x}^\nu}.$$

where $p_\theta = \frac{\partial \mathcal{L}}{\partial \dot{\theta}}$, m is the rest mass of the particle and L_ϕ is the angular momentum along the axis of rotation of the black hole; since we imposed $\dot{\theta} = 0$, the lagrangian is independent from it, so $p_\theta = 0$. Rearranging the equation for E and L we find

$$\dot{t} = \frac{1}{\Delta}\left[\left(r^2 + a^2 + \frac{2a^2M}{r}\right)E - \frac{2aM}{r}L\right], \tag{1.19}$$

$$\dot{\phi} = \frac{1}{\Delta}\left[\left(1 - \frac{2M}{r}\right)L + \frac{2aM}{r}E\right]. \tag{1.20}$$

these will be useful in a bit. Meanwhile we can write the Hamiltonian as

$$\begin{aligned} 2\mathscr{H} &= 2\left[p_t\dot{t} + p_\phi\dot{\phi} + p_r\dot{r} - \mathscr{L}\right] = \\ &= E\dot{t} - L\dot{\phi} - \frac{r^2}{\Delta}\dot{r}^2 = \delta_1 = constant, \end{aligned} \tag{1.21}$$

this obviously has to be conserved throughout the motion. Now we can rearrange the Hamiltonian to express explicitly as follows

$$r^2\dot{r}^2 = r^2E^2 + \frac{2M}{r}\left(aE - L\right)^2 + \left(a^2E^2 - L^2\right) - \delta_1\Delta, \tag{1.22}$$

where we remember that $\Delta = \left(r^2 - 2Mr + a^2\right)$. We are looking for timelike geodesics and this means that we want a positive Hamiltonian, so we choose $\delta_1 = 1$. If it was null, we would have been looking for null geodesics. The equation can be expressed in a more useful way by using the relation $r = u^{-1}$, so it becomes

$$u^{-4}\dot{u}^2 = -\left(a^2u^2 - 2Mu + 1\right) + E^2 + 2M\left(aE - L\right)^2u^3 - \left(a^2E^2 - L^2\right)u^2. \tag{1.23}$$

To find the circular orbit we require the left hand to be null and the right hand to have a double root (so that it will represent either a maximum or a minimum). This way we can obtain

$$E = \frac{1 - 2Mu \mp a\sqrt{Mu^3}}{\sqrt{1 - 3Mu \mp 2a\sqrt{Mu^3}}} \tag{1.24}$$

$$L = \mp\frac{\sqrt{M}}{\sqrt{u\left(1 - 3Mu \mp 2a\sqrt{Mu^3}\right)}}\left[a^2u^2 + 1 \pm 2a\sqrt{Mu^3}\right]. \tag{1.25}$$

After some manipulation we write the angular velocity as follows

$$\Omega = \frac{\dot{\phi}}{\dot{t}} = \frac{d\phi}{dt} = \frac{L - 2Mu(L - aE)}{(r^2 + a^2)\,E - 2aMu(L - aE)} = \frac{\mp\sqrt{Mu^3}}{1 \mp a\sqrt{Mu^3}}. \tag{1.26}$$

For each chosen distance we can compute also the speed which will be

$$v^{\phi} = \frac{\mp\sqrt{Mu}}{\left[1 \mp a\sqrt{Mu^3}\right]\sqrt{\Delta_u}}\left[1 + a^2u^2 \pm 2a\sqrt{Mu^3}\right], \tag{1.27}$$

where $\Delta_u = a^2u^2 - 2Mu + 1$. More details can be recovered on Chandrasekhar 1992. We will make sure that the speed will not go superluminal. The effect of frame dragging has a huge contribution to general geodesic motion. We define prograde and retrograde motion, which means respectively that the orbital angular momentum of the test particle is concorde or discorde to spin of the black hole. When there will be $\pm$ or $\mp$, the top sign will indicate the retrograde and the bottom one the prograde. To carry out this project we computed the retrograde motion, since the results from EHT 2022a suggest that the black hole spin is positive (counter-clockwise), while M. Wielgus et al. 2022 that find the motion to be clockwise.

1.5 Geodesic motion for ray tracing

A light ray generated by the source will be affected by the curvature of the space-time, meaning that an observation of an astrophysical object may not reproduce the effective shape of the body because it will be distorted through light bending. The reproduction of this effect is called Ray Tracing.

Physically, the light generated is scattered in all the directions, so most of the rays will will not head to out detector. In order numerically simulate the process, we will perform a back integration generating the rays from the telescope heading to the source. Our aim is to understand how a black hole with an accretion disk will be imaged.

The most general way is to integrate directly the full geodesic equation, that is formally written as

$$\frac{d^2x^{\mu}}{d\lambda^2} = -\Gamma^{\mu}_{\alpha\beta}\frac{dx^{\alpha}}{d\lambda}\frac{dx^{\beta}}{d\lambda}, \tag{1.28}$$

where λ is the affine paramiter of the curve, while the Christoffel symbols $\Gamma^{\mu}_{\alpha\beta}$ identify the space-time and the coordinate system we are using. These coefficient are generally

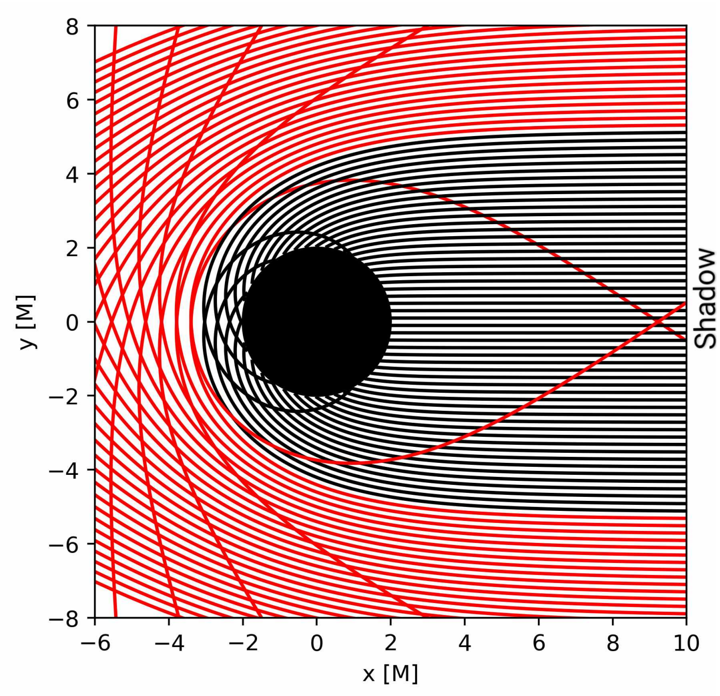

Figure 1.2: Ray tracing of null geodesics in the equatorial plane of a Schwarzshild space-time (described in section 1.2). In black the rays captured inside the event horizon (the black circle), while in red the rays not bounded. The rays are generated all parallel at $x = 200M$, while $-10M < y < 10M$. The black rays compose the shadow, with a radius of $3\sqrt{3}M$.

calculated by hand once we know the background space-time, the general formula reads:

$$\Gamma^{\mu}_{\alpha\beta} = \frac{1}{2} g^{\mu\nu} \left(g_{\nu\alpha,\beta} + g_{\beta\nu,\alpha} - g_{\alpha\beta,\nu} \right), \tag{1.29}$$

where $g_{\nu\alpha,\beta} \equiv \frac{\partial g_{\nu\alpha}}{\beta}$.

Now that we know the equations and how to compute them, we have to understand the conditions: we simulate a camera situated at a large distance, then we generate as many light rays as number of pixels we require for the image.

Fig. 1.2 shows a 2D ray tracing simulation for null geodesics in a more simple, but representative, Schwarzshild space-time as an example. Here we have generated parallel rays changing only the y coordinate in the initial conditions. The black circle represents the event horizon of radius $R_S = 2M$[5]. We can interpetrate the initial value of the y coordinate as an impact parameter. The black rays can have this parameter greater than the horizon radius itself, this means that the effective size of the black hole in the telescope

[5]The mass unit represents the gravitational radius $r_g = \frac{GM}{c^2}$, taking $c = G = 1$.

will be the maximum value of the impact parameter. The effective image of the event horizon seen by an external observer is shadow. For the Schwarzshild case, the shadow is circular with a radius of $3\sqrt{3}M$ (see Chandrasekhar 1992).

Up to now we have considered the space to be empty, meaning that there would be no radiation to measure; while a black hole can be surrounded by matter, treated in general as a gas. The dynamics of gases around a black is not trivial, in the next section we are going to have an idea on how the matter behaves in such situation.

1.6 Gas around a black hole

Observing a black hole means to measure the radiation generated by the gas flowing around it. In our case, the matter (considered to be a fluid) does not contribute to the shape of the space-time, that is only due to the rotating black hole. The matter energy density is in general too little so the right hand of the Einstein equations 1.1 is taken null.

To get a first idea we can say that generally, when a star gets too close to a black hole, it gets disrupted and some of the gas may stay in orbit, slowly closing the distance to the event horizon. The motion of the particle can be arbitrarily complex and it can happen that when going towards the black hole, it gets accelerated and launched in the direction of the rotation axis. The matter orbiting the black hole forms and accretion flow/disk, while the launched matter generates a relativistic jet.

Accretion flows were first derived mathematically in Weizsäcker 1948. It was thought to be a laminar flow [6] but in order to the matter to infall the disk should loose gravitational energy and angular momentum, although the overall angular momentum of the disk has to be conserved; so it is needed a redistribution of such quantity. Later in the century, it was discovered a physical process that could allow for such redistribution; the magnetic fields could be the cause for instabilities and turbulence, slowing down the inner region of the gas Balbus and Hawley 1991. In EHT 2022b it is shown how the observation of Sgr A* is best fitted by a magnetically arrested disk (MAD) (Narayan, Igumenshchev, and Abramowicz 2003). The MAD model describes an accretion flow with a strong poloidal field [7], which can distrupt the flow in 2 concentrical parts where the internal is mostly turbolent, at high fluid velocities. At this point the black hole will accrete through discrete blobs or streams, making the accretion rate much slower that the free fall speed (see Narayan, Igumenshchev, and Abramowicz 2003).

Often happens that accretion flows are followed by an other phenomena: Astrophysical jets. There are highly collimated beams of particles and radiation, we can find them in

[6] A laminar flow is characterized by parallel sheets of fluid that do not allow for meshing or turbulences.

[7] A thick flow can be approximated to have a toroidal shape. On this structure we can define the toroidal and poloidal angle. The first is essentially the azimuthal angle identifying a circular section, while the second rotates on the torus identifying the point on the section.

systems like the one treated here, but they can be associated also to quasars, protostars, neutron stars, pulsar and more. The origin of such object is not yet confirmed but they are thought to be strongly related to the accretion disk. It is not well understood where the particles take so much energy as the jets reveal, first it was believed that the black hole alone could provide such energy, by an extraction process that takes energy from the spin of the black hole (see Abramowicz and Fragile 2013). In Blandford and Znajek 1977 it is shown how the magnetic fields have a huge role because, once the particles get closer to the ergosphere, the magnetic lines becomes so tight that provides a huge torque. The interesting point is that this phenomena is dependent from the black hole spin, the stronger it is, the more torque can be extracted by the magnetic interaction. In this theory the accretion disk is only a sheet of current that provides the magnetic component.

Nowadays we know very little on these phenomena and how they are linked, maybe numerical simulations (like the one provided for this thesis) may be the key. This brief explanation is useful to understand the images shown in the results, we will notice that the emission is provided by the base of the jet that is situated very close to the horizon itself, while we will not be able to see the accretion disk because it will not generate emission intense enough. Now that we get the idea on the structure and how they may be connected, we can try to understand how radiation is influenced by this matter.

–2–
Radiation

To observe astrophysical objects, we rely on detecting their emissions, with a particular focus on electromagnetic radiation. In the following sections, we will delve into the process by which radiation escapes from evolving plasma. Specifically, we will rephrase the classical equation in a covariant form. Subsequently, we will explore the electron distribution function and the mechanisms underlying actual emissions.

2.1 Radiative transfer

When light is emitted from a specific point within a gas, it undergoes multiple scattering events before eventually either reaching an observer on Earth or being absorbed once more. This intricate process implies that not all of the gas present will actively contribute to the observable emission detected from our vantage point. General relativistic formalism provides the framework for formalizing and comprehending this intricate interplay between gravity and radiation. This includes considering the effects of gravitational lensing, time dilation and the alteration of geodesic due to the intense gravitational field near massive objects. The general relativistic treatment of radiative transfer is indispensable in accurately modeling and interpreting the observed emissions from these extreme environments. It aids in understanding how light interacts with matter and gravity in a strong gravity regime, shedding light on the nature of the emissions and the properties of the astrophysical systems under investigation. Formalizing in a general relativistic manner means that the overall shape of the equation will be conserved under coordinate transformation. To obtain this formulation we re-trace the calculations in Younsi, Wu, and Fuerst 2012.

The classical equation for the radiation transfer describes how electromagnetic radiation propagates through a medium. It is commonly known as the Radiative Transfer Equation (RTE) and can be expressed as follows:

$$\frac{dI_\nu}{ds} = -\alpha_\nu I_\nu + j_\nu, \tag{2.1}$$

where s is the path lenght, I_ν is the specific intensity of the radiation, therefore dI_ν/ds represents the change in intensity of radiation at a specific frequency ν as it traverses a differential path length ds. α_ν is the absorption coefficient indicating how strongly the medium absorbs radiation at that specific frequency and j_ν represents the emission coefficient signifying the rate at which radiation is emitted at that frequency per unit volume. The RTE is a fundamental tool in various scientific fields, including astrophysics, atmospheric science, and remote sensing, as it helps explain how radiation interacts with and moves through different materials and environments. It plays a crucial role in understanding phenomena like the behavior of light in stars, the Earth's atmosphere, and many other complex systems involving radiation.

We can define the optical depth

$$\tau_\nu = \int_{s_0}^{s} \alpha_\nu(s')\, ds' \implies d\tau_\nu = \alpha_\nu(s) ds, \tag{2.2}$$

which tells us about the extend to which a light ray penetrates into a medium before it is entirely absorbed or extinguished. In essence, it quantifies the cumulative absorption experienced by the light along its path, providing insights into the material's opacity and the probability of absorption at various points along the ray's trajectory. In astronomical and atmospheric studies, understanding the optical depth is pivotal for interpreting observations, such as the absorption of specific wavelengths by different gases in a planet's atmosphere or the opacity of a stellar interior. It plays a fundamental role in characterizing the behavior of light in diverse environments and is a cornerstone concept in radiative transfer theory. At this point we can reformulate the above equation (2.1) to be

$$\frac{dI_\nu}{d\tau_\nu} = -I_\nu + S_\nu \quad \text{with} \quad S_\nu = \frac{j_\nu}{\alpha_\nu}, \tag{2.3}$$

where S_ν is called the source term. This term is a crucial component of the radiative transfer equation. It represents the emission of radiation at a specific frequency concerning the equilibrium within the medium. More precisely S_ν quantifies the balance between emission and absorption at that frequency. It signifies the rate at which radiation is being actively generated or absorbed within the medium, providing a comprehensive understanding of the radiative processes occurring at that specific frequency. While the optical depth already is a Lorenz invariant because it is a 4-scalar, the specific intensity is not. To solve it, we can start from the definition phase space density

$$f(x^i, p^i) = \frac{dN}{dV}. \tag{2.4}$$

This expression defines the phase space density as the ratio of the change in the number of particles dN to the corresponding change in phase space volume dV. It's important to note that this phase space density is an invariant quantity. This invariance arises because the total number of particles is conserved within a given phase space volume. Using Liouville Theorem, we can further establish that: $\frac{dV}{d\lambda} = 0$. This assertion implies that the phase space volume remains constant as it evolves along the affine parameter λ. In other words, as the system undergoes changes over its trajectory, the volume within phase space, encompassing all possible particle positions and momenta, remains conserved. [1] This quantity can be written explicitly as

$$f(x^i, p^i) = \frac{dN}{dV} = \frac{dN}{dx^i \cdot dp^i} = \frac{dN}{dAdt \cdot E^2 dEd\Omega}, \tag{2.5}$$

where we have used $c = 1$ to write the space element volume. For our purposes, we remember the definition of specific intensity

$$I_E = \frac{EdN}{E^2 dEdAdtd\Omega} \tag{2.6}$$

defined as the energy E per unit time dt, per unit solid angle $d\Omega$, per unit area dA, and per unit energy dE. By combining these definitions, we can introduce a redefinition of the phase space density (2.5) as follows:

$$\mathcal{I} \equiv f = \frac{I_\nu}{\nu^3} = \frac{I_E}{E^3}. \tag{2.7}$$

This redefinition it can be used to rewrite the radiative transfer equation as:

$$\frac{d\mathcal{I}}{d\tau_\nu} = -\mathcal{I} + \mathcal{S} \quad \text{with} \quad \mathcal{S} = \frac{\eta}{\chi} = \frac{S_\nu}{\nu^3}, \tag{2.8}$$

where we have defined two crucial quantities: $\eta = \frac{j_\nu}{\nu^2}$ which represents the invariant rate of radiation emission per unit frequency and $\chi = \nu\alpha_\nu$ which signifies the invariant product of frequency and absorption coefficient. Since these are invariant quantities for Lorentz transformations, the local rest frame, denoted by "0", will held[2] $\chi = \nu\alpha = \nu_0\alpha_{0\nu}$

[1] This conservation of phase space volume is a fundamental concept in the study of dynamical systems and has profound implications in various branches of physics, particularly in the context of Hamiltonian mechanics and the preservation of particle trajectories.

[2] This invariance underlines the significance of these parameters in the context of radiative transfer and

and $\eta = \frac{j_\nu}{\nu^3} = \frac{j_{0\nu}}{\nu^3}$. The best way to implement this equation in a code is to separate the Lorentz invariant intensity and the optical depth into two equations, it is done by introducing the affine parameter λ. In doing so we will use the 4-momentum of a photon in the comoving frame, denoted as v^α defined by the equations:

$$v^\alpha = k^\alpha + (k_\beta u^\beta)u^\alpha. \tag{2.9}$$

Here u^α is the 4-velocity of the fluid and k^α is the 4-momentum of the photon. We have also introduced the projection tensor $P_{\alpha\beta} = g^{\alpha\beta} + u^\alpha u^\beta$, meaning that we are projecting our vectors on the comoving coordinate system. Now, we can explicitly express the proceed by explicitating the following derivative

$$\frac{ds}{d\lambda} = -||v^\alpha||_{\lambda_{obs}} = -(k_\alpha u^\alpha)_{\lambda_{obs}}, \tag{2.10}$$

where we have used that $k^\alpha k_\alpha = 0$ and $u^\alpha u_\alpha = -1$. Now if we remember that the contraction $p_\mu u^\mu = -E$, we can relate the above derivative to the relative energy shift, γ^{-1}, which is given by

$$\gamma^{-1} = \frac{\nu_0}{\nu_{obs}} = \frac{E_\lambda}{E_{\lambda_{obs}}} = \frac{(k_\alpha u^\alpha)_\lambda}{(k_\alpha u^\alpha)_{\lambda_{obs}}}. \tag{2.11}$$

If we normalize the observed energy as observed at infinity ($E = 1$) we get that the energy shift is

$$\gamma^{-1} = -(k_\alpha u^\alpha)_{\lambda_{emiss}}. \tag{2.12}$$

Now we have the instruments to re-write the equation (2.8). First, we decouple the specific intensity from the optical depth as follows:

$$\frac{d\tau_\nu}{ds} = \alpha_\nu, \qquad \frac{d\mathcal{I}}{ds} = \alpha_\nu \mathcal{I} + \frac{j_\nu}{\nu^3}. \tag{2.13}$$

After some algebraic manipulation, we can reformulate the equations as:

$$\frac{d\tau_\nu}{d\lambda} = \gamma^{-1}\alpha_{0\nu}, \qquad \frac{d\mathcal{I}}{d\lambda} = \gamma^{-1}\left(\frac{j_{0x\nu}}{\nu^3}\right)e^{-\tau_\nu}. \tag{2.14}$$

In these reformulated equations, we've effectively separated the effects of intensity and optical depth, allowing for a more efficient computational implementation. These equations are particularly useful when modeling radiative transfer processes in various physical contexts.

their applicability across various physical scenarios, regardless of relativistic transformations.

2.2 Thermal and non-thermal emission

In the pursuit of our scientific aim, it is essential to reiterate our overarching objective: we endeavor to simulate a plasmoid formation, a phenomenon we hypothesize to be generated through the intricate process of magnetic reconnection. To accurately represent and understand this plasmoid's behavior and its associated emissions, we must account for the significant magnetic contributions that permeate the system and affect particle dynamics. To address this magnetic influence effectively, we turn our attention to a particle distribution model influenced by the magnetic field – the kappa distribution. This distribution has garnered considerable attention and empirical support within the realm of astrophysics. It has been extensively explored and validated in a variety of astrophysical scenarios, including solar emissions (Vasyliunas 1968, Pierrard and M. Lazar 2010) and the complex dynamics of Earth's magnetosphere (Eyelade et al. 2021). Notably, the kappa distribution has found relevance in understanding emissions from extragalactic sources as well. For instance, in the study by Fromm et al. 2022, researchers probed the impact of non-thermal electron distributions, which are aptly described by the kappa distribution, on the emissions emanating from the M87 supermassive black hole. A similar exploration was undertaken in EHT 2022b, focusing on the emissions originating from Sgr A*, the supermassive black hole located at the center of our Milky Way galaxy. These investigations consistently demonstrated that the most accurate representations of observed emissions often necessitate a combination of thermal and non-thermal electron populations, highlighting the versatility and applicability of the kappa distribution in diverse astrophysical contexts. In the specific context of this section of our research, our objective is to delve into the phenomenon of synchrotron emission. Synchrotron emission is a fundamental radiation mechanism prevalent in various astrophysical environments. It manifests when charged particles, typically electrons, are set into spiraling motion within magnetic fields, emitting copious amounts of electromagnetic radiation in the process. Our approach is to incorporate both thermal and kappa-distributed electron populations. This treatment is essential for capturing the complex interplay between magnetic reconnection, particle distributions, and the subsequent radiation processes that shape the emissions from the plasmoid. By pursuing this multifaceted approach, we aim to construct a more comprehensive and realistic simulation of the plasmoid's behavior and emissions, thereby shedding light on the intricate astrophysical processes governing these phenomena.

Plasma-β: In the process of calculating emission characteristics, particularly within the context of General Relativistic Magnetohydrodynamics (GRMHD) simulations, it is often essential to determine the electron temperature. However, GRMHD simulations primarily track proton dynamics, providing us with comprehensive data on parameters such as temperature, density, and pressure pertaining to protons. To bridge the gap and obtain the electron temperature, a conversion model is required, as proton temperature and electron temperature are not inherently equivalent. In this regard, we have adopted the widely employed plasma-β model, as detailed in Fromm et al. 2022 and Moscibrodzka, Falcke, and Shiokawa 2015.

The plasma-β model stands as an alternative choice to the standard constant ratio between electron temperature and proton temperature. This model has been successfully used for solar atmospheric physics (see Gary 2001), it is able to better capture the influence of the magnetic field on the electrons. The dimensionless electron temperature Θ_e is the key parameter that will be exploited in the simulation, it is defined as follows

$$\Theta_e = \frac{p}{\rho}\frac{m_p T_e}{m_e T_p}, \qquad \frac{T_p}{T_e} = \frac{R_{low} + R_{high}\beta^2}{1+\beta^2}. \tag{2.15}$$

Here p represents the barionic pressure, ρ is the barionic density„ m_p and m_e denote the proton and electron masses, respectively, and T_e and T_p are the electron and proton temperatures. The parameter $\beta = p_{gas}/p_{mag} = 2p/b^2$ is the ratio between gas and magnetic pressure. The variable b^2 represents the module of the magnetic field 4-vector b^μ, this is defined as

$$b^t = B^i u^\mu g_{i\mu} \qquad b^i = \frac{B^i + b^t u^i}{u^t},$$

where we call B^i the 3-vector of the magnetic field and u^i is the 4-velocity. The parameters R_{low} and R_{high} represent respectively the ratio between proton and electron temperature at $\beta = 0$ (high magnetization) and $\beta \longrightarrow \infty$ (low magnetization), they can be considered boundary conditions for function. As shown by Fromm et al. 2022, R_{high} does not affect the emission in high magnetized plasma, on the opposite it influences the disk making the electron temperature lower, decreasing the Lorentz factor γ , making the disk dimmer. On the other hand, R_{low} has the role of establishing the electron temperature in the high magnetization region, so the jet, meaning that an higher value implies for higher electron temperature allowing for a longer and broader jet. In this study, these two parameter are set at $R_{low} = 1$ and $R_{high} = 160$, trying to force less energetic electrons. The plasma-β model, with its foundation on magnetization levels, is preferred in performing simulation especially in scenarios where magnetic fields exert a significant influence.

Thermal electron distribution function: To characterize the thermal electron distribution function, we rely on the relativistic Maxwell-Juttner distribution, which is expressed as (Fromm et al. 2022):

$$\frac{dn_e}{d\gamma_e} = \frac{n_e}{4\pi\Theta_e}\frac{\gamma_e\sqrt{\gamma_e^2 - 1}}{K_2({}^1\!/_{\Theta_e})} exp\left(-\frac{\gamma_e}{\Theta_e}\right), \tag{2.16}$$

where n_e is the electron density, γ_e is the Lorentz factor of the electron, K_2 is the Bessel function of 2nd kind. Here the electron temperature is classically defined as $\Theta_e = \frac{k_B T_e}{m_e c^2}$, where κ_B is the Boltzmann constant, T_e is electron temperature, m_e is the electron mass, and c is the speed of light. The relativistic Maxwell-Juttner distribution serves as a special-relativistic extension of the classical Maxwell distribution function. It is particularly valuable in scenarios involving high-energy electrons, where relativistic effects become significant. Notably, this distribution function exhibits convergence in the low-temperature limit ($T \ll {}^{m_e c^2}\!/_{k_B}$), demonstrating its versatility and applicability across a wide range of temperature regimes. By employing the electron temperature defined within the plasma-β model, we ensure that our distribution function remains consistent with the broader astrophysical framework, enabling a comprehensive description of thermal electron behavior in a relativistic context.

Non-thermal electrons, Kappa distribution function: The kappa distribution function here described is the maximum for the Tsallis non-extensive entropy (Livadiotis and McComas 2009). This distribution function provides a robust representation of non-thermal electron populations characterized by power-law tails. It is expressed as:

$$\frac{dn_e}{d\gamma_e} = \frac{N}{4\pi}\gamma_e\sqrt{\gamma_e^2 - 1}\left(1 + \frac{\gamma_e - 1}{\kappa w}\right)^{-(\kappa+1)}. \tag{2.17}$$

Here, N is a normalization factor (more details in Pandya et al. 2016), κ is related to a power law exponent characterizing the distribution. The energy content of this distribution is determined by the width w, encompasses contributions from both thermal energy and a fraction ϵ of the magnetic energy. Readly, the width is

$$w := \frac{\kappa - 3}{\kappa}\Theta_e + \frac{\epsilon}{2}\left[1 + \tanh\left(r - r_{inj}\right)\right]\frac{\kappa - 3}{6\kappa}\frac{m_p}{m_e}\sigma,$$

in which we indicate as r_{inj} the distance where we start to inject electrons with magnetic contributions. The magnetic component is accounted for by the parameter $\sigma = {}^{b^2}\!/_{\rho}$ which is the plasma magnetisation. The variable κ is defined as

$$\kappa := 2.8 + 0.7 \cdot \sigma^{-1/2} + 3.7 \cdot \sigma^{-0.19}\tanh(23.4\sigma^{0.26}\beta). \tag{2.18}$$

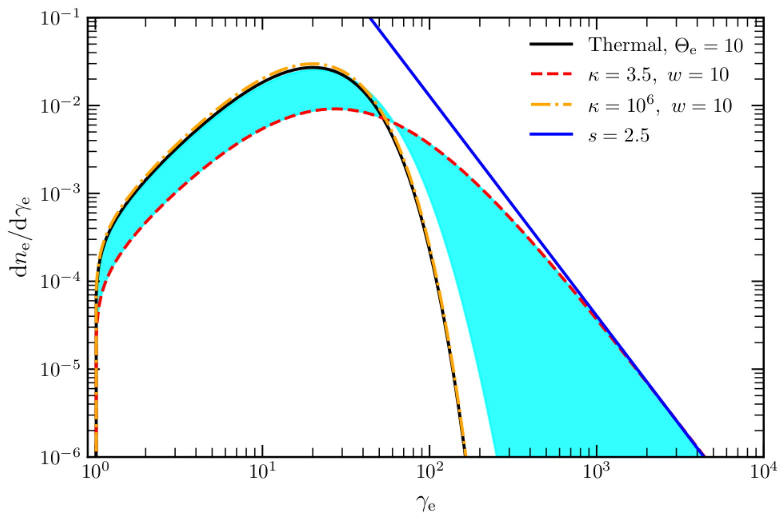

Figure 2.1: Representation from Fromm et al. 2022. Comparison between the Maxwell-Juttner distribution function (in black), a power low ${dn_e}/{d\gamma_e} =\propto \gamma_e^{-s}$ (in blue) and the kappa distribution (dashed lines in yellow and red).

It is worth noting that the choice of κ significantly influences the shape of the distribution (see fig. 2.1). A larger value of κ such as $\kappa = 10^6$ closely approximates the exponential decay characteristic of a thermal distribution. In contrast, the general behavior of the kappa distribution tends to produce flatter distributions, allowing for a broader range for a broader range of the Lorentz factor γ_e to be included in the emission. The versatile kappa distribution is particularly well-suited for describing non-thermal electron populations in various astrophysical contexts, offering a flexible framework to capture the complex interplay between particle dynamics, magnetic fields, and emission processes. This distribution allows us to model scenarios where non-thermal electron contributions are significant and offers valuable insights into the spectral properties of the emitted radiation. For further visual clarity, please refer to Figure 2.1 for a visual representation of the distribution characteristics.

Emissivity and absorbtivity: In the realm of astrophysical emissions, it is essential to consider the polarization of radiation. Normal bremsstrahlung emission, which occurs when charged particles are accelerated within a plasma, typically results in randomly polarized radiation. This randomness arises from the stochastic nature of the particle accelerations, leading to emissions that exhibit no preferred polarization direction. However, observations often reveal highly polarized emissions, indicative of a different physical process at play. This departure from random polarization hints at the presence of synchrotron emission. Synchrotron radiation exhibits a distinct polarization signature because it arises from the motion and acceleration of relativistic particles within a magnetic field. In synchrotron emission, the polarization direction aligns with the orientation of the magnetic field. This is a consequence of the fact that all scattering events, responsible for emitting synchrotron radiation, occur in the presence of the same magnetic field. As a result, the emitted radiation exhibits a preferred polarization direction. The presence of polarization in observed emissions serves as a key indicator of the underlying emission mechanism. We are not yet able to provide polarization transport with the available sources, nevertheless we study the intensity of the emission.

The emission and absoption coefficients are computed as in Pandya et al. 2016. In the context of synchrotron emission in a vacuum, these processes exhibit a universal mathematical form. To characterize this emission, we define $\nu_c = \frac{eB}{2\pi m_e c}$ that represents the characteristic synchrotron frequency. The constants e and m_e are respectively the electron charge and mass, while B is the module of the magnetic field and c is the light speed. Two key parameters, j_S and α_S, can be expressed as:

$$j_S = \frac{n_e e^2 \nu_c}{c} J_S\left(\frac{\nu}{\nu_c}, \theta\right), \qquad \alpha_S = \frac{n_e e^2}{m_e \nu c} A_S\left(\frac{\nu}{\nu_c}, \theta\right). \tag{2.19}$$

Here j_S represents the intensity of the synchrotron emission,α_S denotes the absorptivity of the emitted radiation, and the adimensional functions A_S and J_S are functions of various parameters including the electron temperature Θ_e and the w, κ (for the kappa model). The index S is particularly relevant when considering polarization, but in our context, we are primarily interested in the first index, $S = I$ which represents the intensity of the emission. It is worth noting that the full computation of these quantities using the general formula can be computationally expensive. Hence, we often rely on approximated fitting formulas based on research by Pandya et al. 2016 and Leung, Gammie, and Noble 2011. If we introduce the variable $X = \frac{\nu}{\nu_c}$ we can write the a adimensional function in 2.19 as

$$j_{Thermal} = e^{-1/3} \frac{2\pi}{27} \sin\theta \left[X^{\frac{1}{2}} + 2^{\frac{11}{12}} X^{\frac{1}{6}}\right]^2, \tag{2.20}$$

$$j_{kappa} = \left(J_{I,lo}^{-3\kappa^{-3/2}} + J_{I,hi}^{-3\kappa^{-3/2}}\right)^{\frac{1}{3\kappa^{-3/2}}}, \tag{2.21}$$

respectively for thermal and kappa distribution. In the latter, the two addends corresponds respectively for low and high frequency, explicitly

$$J_{I,lo} = X_\kappa^{1/3} \sin\theta \frac{4\pi\Gamma(\kappa - 4/3)}{3^{\frac{7}{3}}\Gamma(\kappa - 2)}, \tag{2.22}$$

$$J_{I,hi} = X_\kappa^{-\frac{\kappa-2}{2}} \sin\theta\, 3^{\frac{k-1}{2}} \frac{(\kappa-2)(\kappa-1)}{4} \Gamma\left(\frac{\kappa}{4} - \frac{1}{3}\right)\Gamma\left(\frac{\kappa}{4} + \frac{4}{3}\right). \tag{2.23}$$

Here $X_\kappa = X/(w\kappa)^2$ and $\Gamma(x)$ is the gamma function. Detailed expressions for these functions are provided in equations (2.22) and (2.23). It's important to note that these formulas capture the essence of synchrotron emission across a range of frequencies and magnetic field strengths, making them invaluable tools for characterizing astrophysical emissions. The absorptivity α_ν for the thermal case is calculated straightforwardly as $\alpha_\nu = j_\nu/B_\nu$, where B_ν represents the black body emission according to Kirchhoff's law. For the kappa distribution, the absorptivity is similar to the emissivity (equation 2.21), with adjustments to the exponents and functions for low and high frequencies, as detailed in reference Pandya et al. 2016 equations (39-42). These formulas provide a robust framework for modeling and understanding synchrotron emissions in astrophysical contexts.

–3–
Method

3.1 The toy model

In this project, we have developed a simplified model to simulate a plasmoid orbiting a black hole. The plasmoid is represented as a spherical object positioned at a distance r_{hp} from the black hole center, with a maximum radius of $R = 2.5M$, where M is the black hole's mass. We are interested in modeling the emission of this plasmoid concerning the surrounding gas. The computation of the absorptivity (α_{hp}) and emissivity (j_{hp}) consists of a Gaussian profile cutted at the maximum radius R as follows:

$$\alpha_{hp} = \alpha_{gas} \cdot A \cdot e^{-\frac{|\vec{r}-\vec{r}_{hp}|^2}{2\sigma^2}} \Theta(R - |\vec{r} - \vec{r}_{hp}|) \qquad \text{for absorptivity,} \tag{3.1}$$

$$j_{hp} = j_{gas} \cdot A \cdot e^{-\frac{|\vec{r}-\vec{r}_{hp}|^2}{2\sigma^2}} \Theta(R - |\vec{r} - \vec{r}_{hp}|) \qquad \text{for emissivity,} \tag{3.2}$$

where α_{gas} represents the absorptivity and j_{gas} represents the emissivity of the surrounding gas, A is a constant factor, $|\vec{r} - \vec{r}_{hp}|$ denotes the relative distance to the plasmoid center $\vec{r}_{hp}$, σ controls the spatial distribution of the Gaussian, and $\Theta(R - |\vec{r} - \vec{r}_{hp}|)$ is the Heaviside step function ensuring that the computation is restricted to within the plasmoid radius R.

It's important to note that these computations are performed exclusively within the hotspot[1], as indicated in the formulation. To perform the simulation, we employed the BHOSS code to compute the ray-traced images, allowing us to visualize the emission characteristics of the plasmoid near the black hole.

[1] Out of completeness, the shape of the hotspot is arbitrary (astrophysical plasmoids, simulated numerically, have been found to have a stable configuration in a spheroidal shape Aimar et al. 2023).

3.2 Ray tracing

Ray tracing is a computational technique employed to trace the paths of electromagnetic signals back to their sources. In this context, it plays a pivotal role in the observation and analysis of black holes. The fundamental equation governing the process is denoted as 1.28. When a ray encounters the event horizon of a black hole or manages to escape to infinity without being absorbed, the corresponding pixel in the image is represented as black. However, a ray can also be absorbed by the gas that surrounds the black hole, and this absorption phenomenon hinges on the optical depth of the gas, a critical parameter described in (2.14). For a more comprehensive understanding of optical depth, please refer to Section 2.1.

The resulting image is generated to get a specific frequency of detection, in our case, fixed at 230GHz. Nevertheless, the light ray at the emission will have the same frequency due to the gravitational redshift. In order to find the emission frequency, we use the energy shift γ^{-1} calculated in equation 2.12; we can clearly see that this way, the frequency of emission will be

$$\nu_{emiss} = \nu_{detected} \cdot \gamma^{-1}. \tag{3.3}$$

Once we have the emission frequency, we can compute the intensity as shown in section 2.2, where the other parameters are either set by the user as initial condition or computed directly from the General Relativistic Magneto Hydrodynamics (GRMHD) data.

Once the initial intensity is calculated, we have to integrate eq. 2.8 along the geodesic in order to infer its value at the camera position.

3.3 Initial conditions of the simulations

Regarding the ray tracing parameters, the camera is set to be fixed at a distance of $2000M$ with an angle of 30^o with respect to the axis of symmetry. This way, we set a long distance to imitate ours while the angle reflects the angle of the equatorial plane with the plane of the sky. The values $R_{high} = 160$, $R_{low} = 1$ and $\sigma_{cut} = 1$ where the latter allows us to neglect the very high magnetization (the jet), saving some computational resources. On the model, we forced the maximum radius of the hotspot to be $2.5M$ because of previous work that constrains the dimensions of such an object and because it may be unreasonable to have such a big object that almost crosses the ergosphere.

3.4 Workflow

In our pursuit of exploring the parameter space within our toy model, we must embark on a well-structured journey, starting with some crucial considerations. The paramount goal is to ensure that each simulation run genuinely represents a physical scenario, adhering as closely as possible to the limits of our model. This endeavor is particularly pertinent as we aim to harmonize the observable quantities derived from our simulations with real-world observations. To achieve this alignment, we employ a systematic approach:

1. **Normalization of Emission:** The cornerstone of our journey begins with aligning our simulated results with actual observations. We need to adjust a pivotal parameter known as the mass accretion rate [2] $\dot{M}$ to ensure that our average emission matches observations, aiming for a target of $\overline{S}_{tot} = 2.4Jy$. The mass accretion rate signifies the amount of gas accreting onto the black hole per unit of time. In our model, it plays a central role in calculating and re-normalizing the electron number density used in emission and absorption functions. The adjustment is made using a straightforward bisection method, ceasing the process when the difference $\Delta\overline{S}_{tot}$ between simulated and observed emission falls below 10^{-7}.

2. **High-Resolution Simulations:** Once we have determined the appropriate mass accretion rate, we proceed with high-resolution simulations. These simulations employ a grid consisting of 200 pixels per side. The high resolution allows us to perform a qualitative comparison with actual observations, essential for accurately computing light curves. or the evolution, we also computed images with a Gaussian filter to simulate the resolution of EHT (that is $25\mu s$)

3. **Resolution Considerations:** We meticulously consider the influence of image resolution in our computational workflow. While high-resolution simulations yield finer details, they also demand more computational resources. It is essential to ensure that the overall flux received remains consistent across different resolutions. On average, increasing the resolution by a factor of 5 results in approximately a $\sim 1.6\%$ increase in the average flux, with a variance of 0.15% of the average. This is deemed an acceptable variation for our study and reaffirms that our estimations of $\dot{M}$ can be confidently made at lower resolutions without compromising the study's overall results.

4. **Parameter Exploration:** Having established a solid foundation with accurate $\dot{M}$ estimations, we delve into the exploration of the four free parameters in our

[2] The mass accretion rate $\dot{M}$ represents the amount of gas that is accreting the black hole. In our model, it is used to calculate and re-normalize the electron number density that the emission and absorption function takes as input, see eq (2.19). In these terms, it quantifies the amount of the gas relative to the mass of the black hole. The gas is mostly made from protons, so it allows the conversion into it into electron density.

model: σ, r_{ph}, A and ε. These parameters are systematically varied and studied, with the ensuing results comprehensively detailed in the following chapter. To further our understanding of our toy model and its alignment with real-world observations, we must assess the model's capability to reproduce variability akin to natural astrophysical phenomena. To study the impact of the hotspot on this variability, we compute differences in light curves with and without the hotspot, defining the variability as indicated by Equation (**??**). This measure allows us to scrutinize the influence of the hotspot parameter on the observed variability. The initial phases of our workflow entail substantial computational demands, primarily due to the iterative nature of the algorithm, which requires multiple simulations until convergence is achieved. Consequently, these initial runs are conducted at lower image resolutions and with a reduced frequency of snapshots (1 out of every 3). However, it is crucial to emphasize that the flux received remains consistent across different resolutions. While the average flux experiences an increase of approximately 1.6% with higher resolutions, this effect is considered acceptable for our study, as it does not compromise the overall results. Moreover, considering the four parameters under examination and assessing the variance in the mean across cases, which amounts to 0.15% of the average, we establish that estimating $\dot{M}$ at lower resolutions is a valid approach, especially given its independence from the hotspot parameter and its minimal interference with the study's objectives. Subsequently, armed with a calibrated model, we embark on high-resolution simulations.

–4– Results

In this Chapter, we present and delve into the results of our analysis. Let's begin by summarizing the primary objectives of our study:

1. **Toy Model Overview:** Our approach involves employing a toy model to simulate various aspects, including near-infrared (NIR) flares Marrone et al. 2008, Eckart et al. 2006, images generated by the Event Horizon Telescope (EHT) collaboration EHT 2022a, and astrometric data provided by the GRAVITY collaboration GRAVITY Collaboration, Bauböck, M., et al. 2020, wherever possible. We aim to investigate how different parameters within our toy model influence both the light curve and the resulting image.

2. **Light Curve Characteristics:** Our ideal light curve exhibits maximum variation, preferably around $1Jy$, within the time range of approximately $200M$ (which equates to roughly one hour because $1M \sim 20s$). Additionally, we anticipate observing variability on shorter timescales, inspired by observations in Maciek Wielgus et al. 2022, where an overarching pattern is followed by smaller-scale fluctuations.

3. **Resemblance to Observations:** We also seek snapshots that can effectively encapsulate the time-averaged observations for Sgr A*.

Before delving into the specifics, it's essential to introduce a concept that will prove instrumental in our subsequent discussions. We've observed that the brightness of the hotspot has a direct impact on the variability of light curves. This relationship arises because the plasmoid's brightness depends on the surrounding background gas, making it position-dependent. Furthermore, we've implemented an algorithm to maintain the average total flux, which means that as the hotspot's contribution to the total flux increases, the contribution from the background gas decreases due to the lower mass accretion rate. Consequently, when the influence of the gas is diminished, we witness a flux that becomes highly dependent on the plasmoid itself, resulting in greater variability. Conversely, a substantial contribution from the background gas leads to a more stable flux over shorter timescales. This intriguing interplay between the hotspot's brightness, the background gas, and the mass accretion rate offers valuable insights. These considerations will be central to our subsequent analysis, shedding light on the intricate dynamics of the plasmoid-black hole system and its manifestations in observations.

In the following panels (e.g. fig.4.1) are shown comparisons between each simulation. Each simulation will be presented, followed by the blurred counterpart, while on the bottom, there will be shown the total flux over the image through time. The hotspot will be highlighted as a brighter region on the top of the black hole. The figures will show snapshots at different times to maximize the visualization of the hotspot to the reader. The proper analysis has been carried out by physical consideration and maximizing either the brightness or the ability to highlight the hotspot region. The blurred snapshots are equipped with level lines at $10^{-2} Jy$ (in blue) and $1.6 \times 10^{-2} Jy$ (in yellow) to highlight the overall structure of the visualized radiation and the brighter spots, respectively.

Effective width - σ

In fig. 4.1, we show the impact of different values of the σ parameter (which we will call effective width) on the simulation. For this analysis, we held other parameters constant, specifically $r_g = 5M$ (representing the gravitational radius), $A = 2.0$, and employed a thermal electron distribution function. We found that the effective width, unsurprisingly, has the most significant impact as it increases in magnitude. As one might intuit, larger values of σ tend to exert a more pronounced emission. In particular, we observed that a value of $\sigma = 2M$ shows the clearest hotspot; for this reason, it will be the fixed value for the following simulation. Moreover, it's worth noting that the variability in the simulation clearly escalates with increasing values of the effective width. These results underscore the critical role of the effective width parameter in shaping the outcomes of our simulation. The careful selection of this parameter can substantially affect the simulation's ability to replicate observed images and variability patterns. This insight informs our ongoing quest for a comprehensive understanding of the plasmoid-black hole system and its manifestations in observed data.

Distance - r_{hp}

So, we fixed $\sigma = 2.0M$ and analyzed the impact of the distance parameter. We also increase the intensity to be $A = 8.0$ because, in this phase of the study, we want to emphasise the effect to better distinguish the cases. Before choosing the values, we have to understand how close to the black hole we can push this object without intersecting

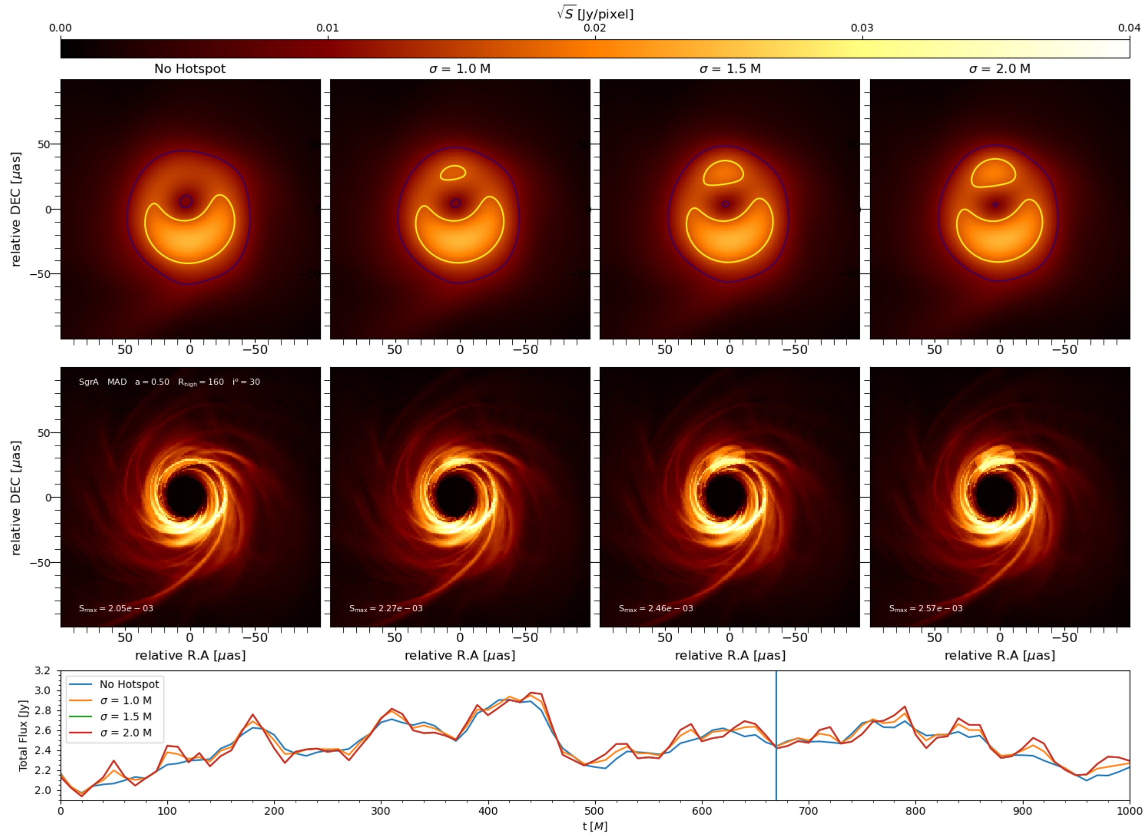

Figure 4.1: In this plot, we visually show the influence of varying effective width values on the simulation outcomes. The set of 2D images displayed from left to right comprises scenarios with different configurations: one without the hotspot, $\sigma = 1M$,$\sigma = 1.5M$, and $\sigma = 2M$. For each of these cases, we provide both the image and its counterpart, which has been purposefully blurred to emulate the resolution limitations of the telescope. The hotspot is situated on the top side of each image. To complete this representation, the lower section of the image presents the corresponding light curves for each of these scenarios.

with the ergosphere. To see this, we plot we use the formula 1.7 obtaining that on the equatorial plane $r_{z+}(a = 0.5M) \sim 1.86M$. This means we cannot place the hotspot closer to $\sim 5M$. Still, we can consider a limit case of $4M$ because the effective width we chose is $2M$. We analyzed many values for the radius from 4M all the way to 12M, but in the figure, we show only the cases 4M, 6M, and 8M that seem to be the most representative to study. This is shown in fig 4.2. Here, it is not clear how this parameter influences the light curve. To have an insight, we can look at 4.3. We can clearly distinguish the various cases since the variability due to the hotspot is isolated. As predicted by the reasoning at the beginning of this chapter, the variability increases as the brightness of the hotspot with respect to the gas. In the case $r_{hp} = 4M$, the hotspot has very high variability. In 2

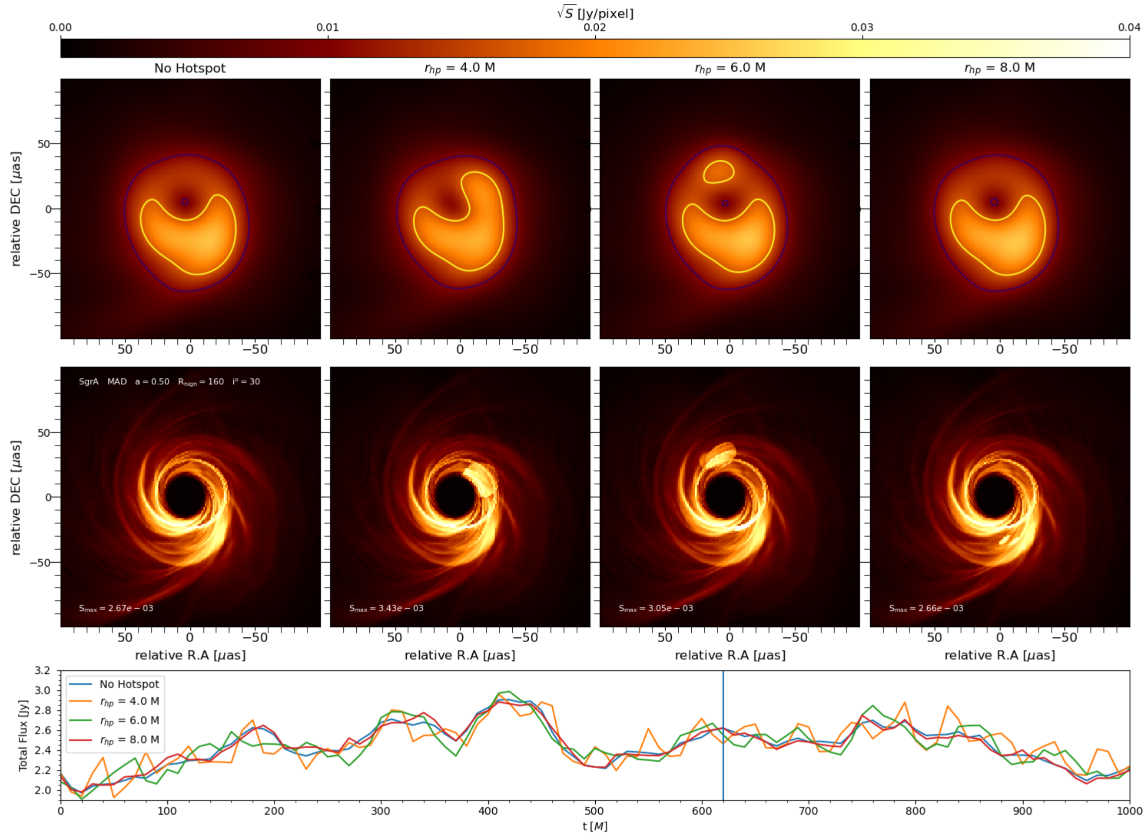

Figure 4.2: This image shows different values of the distance from the black hole. Regarding the 2D images, from left to right there is shown the case without the hotspot, $r_{hp} = 4M$,$r_{hp} = 6M$,$r_{hp} = 8M$. Each case represents the direct image and the blurred one, simulating the resolution of the telescope. The hotspot is located on the right side for the case of $4M$, on the top side for the case of $6M$ and on the bottom (although not visible). On the bottom, it is shown the light curve for each case.

following snapshots, the contribution can change up to $\sim 15\%$ of the total flux. We prefer a more continuous signal like the case of 8M, but with this value, we notice from the images that the hotspot almost disappears, so we take the value 6M to run. We expect that lowering the amplitude will also lower the short-term variability to have a more continuous signal. To understand why the hotspot disappears, we look at a side image of the simulation without the hotspot in Fig. 4.4, in this view, the equatorial plane is complanar to the vertical axes of the image. The distance of $8M$ corresponds to $\sim 40\mu s$ ($1M \sim 5\mu s$, see EHT 2022a), so the plasmoid will be in the middle between the black and the coloured region (at the initial). This is why the hotspot will slowly disappear when we get far from the black hole. This pattern repeats also with other types of emission, so we choose the value $r_{hp} = 6M$ that is in the middle of staying too close or too far.

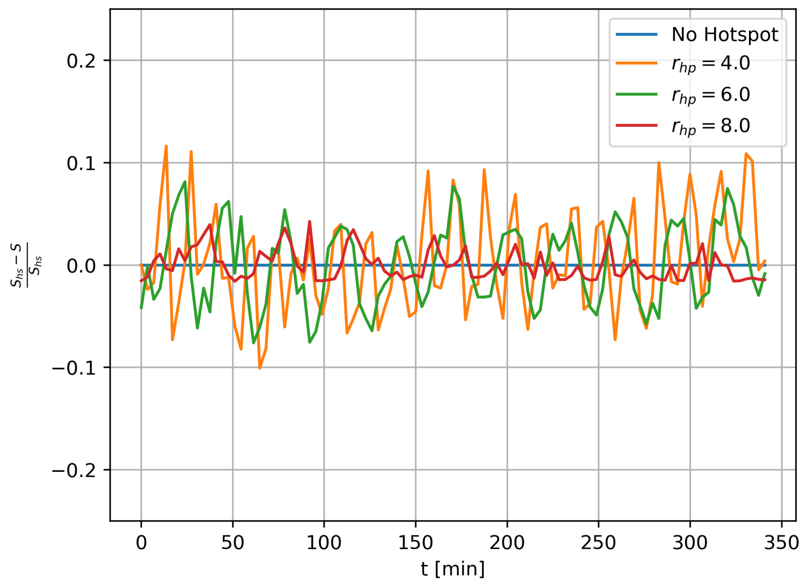

Figure 4.3: Here it is shown, the time in minutes on the x-axis and the variability.

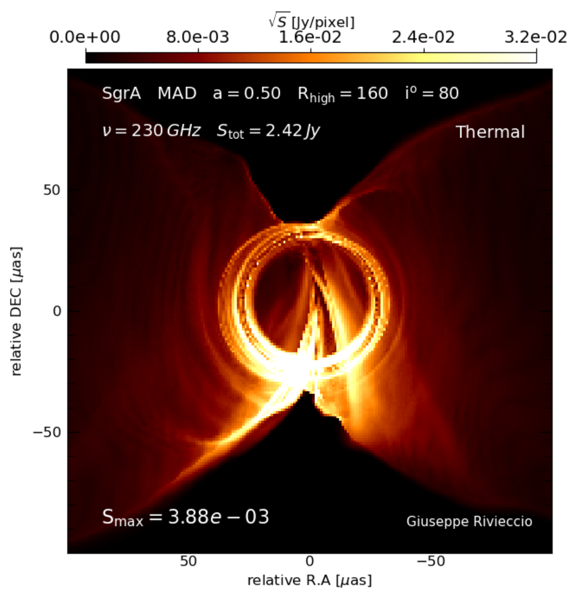

Figure 4.4: Side image of the black hole simulation at inclination $i = 80^o$. Here, it is shown only the detecting frequency 230GHz.

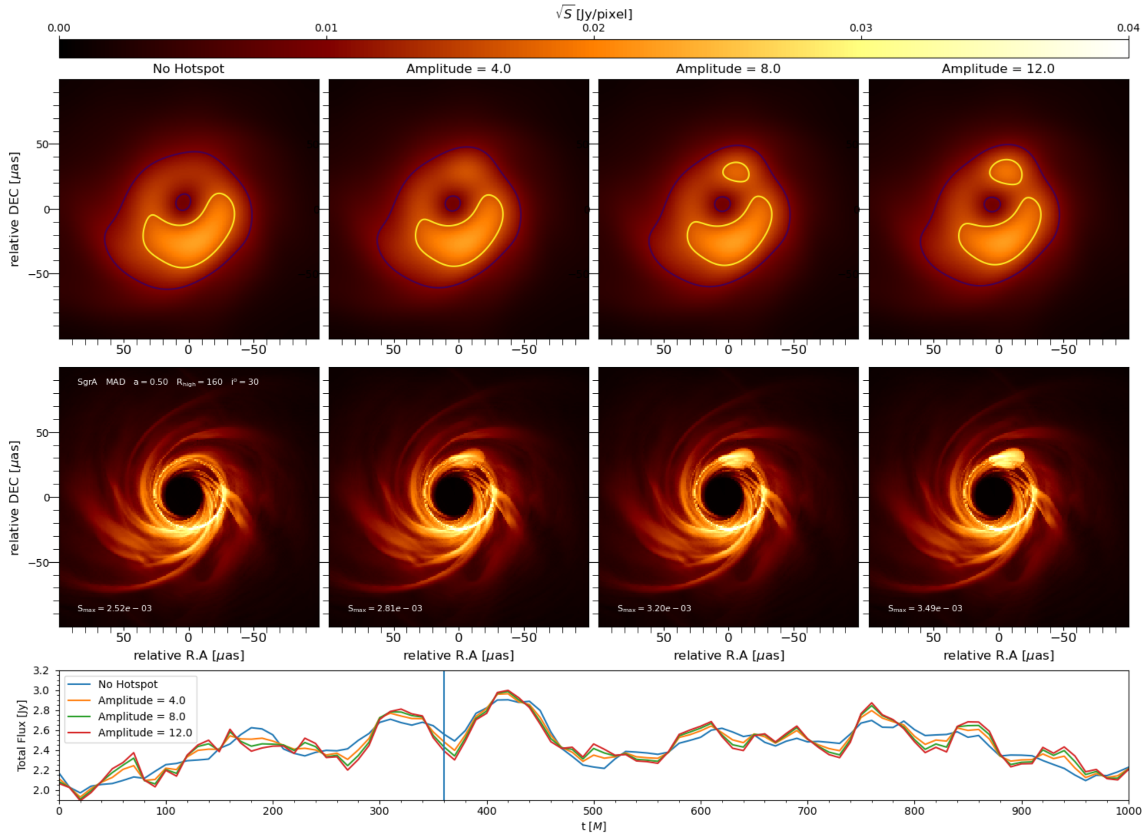

Figure 4.5: On the top side, from left to right, there is shown the case without the hotspot, $A = 4$,$A = 8$,$A = 12$. Each case represents the direct image and the blurred one, simulating the resolution of the telescope. The hotspot is situated on the top side of each image. On the bottom, it is shown the light curve for each case.

Amplitude - A

Here, we explore the influence of amplitude while keeping $\sigma = 2M$, $r_{hp} = 6M$ and utilizing the thermal electron function. We expect that amplitude will play a significant role in both the variability and visibility of the image, much like the effective width. As depicted in Fig. 4.5, it is noticeable that the greater the amplitude, the more pronounced the visibility of the hotspot in relation to its surroundings and the higher the expected variability. Considering the blurred image designed to simulate observations made by the EHT, we expect the hotspot to contribute nearly as prominently as the bright regions in the surroundings. Among the cases considered, it stands out as the most favourable. It is the only case where it becomes possible to discern three distinct bright points.

Magnetic fraction - ε

We now delve into the examination of a crucial parameter that exerts an influence on the emission not only from the hotspot but also from the entire gas region: ε, representing the magnetic fraction. This parameter signifies the portion of magnetic energy incorporated within the electron fraction. Specifically, we refer to the kappa electron distribution function 2.17, characterized by a power law tailed where w represents the width of the distribution peak. The formula is 2.18 as follows:

$$w := \frac{\kappa - 3}{\kappa}\Theta_e + \frac{\epsilon}{2}\left[1 + \tanh\left(r - r_{inj}\right)\right]\frac{\kappa - 3}{6\kappa}\frac{m_p}{m_e}\sigma.$$

The magnetic fraction ε augments the magnetization contribution arising from σ and integrates it with the width of the peak. In the final model selection, his function will undoubtedly take precedence over the thermal component. This is because a plasmoid's generation necessitates the interaction of a magnetic field with matter, necessitating the inclusion of magnetic energy in the emission production. Regarding the hotspot, we have set the parameters as follows: $\sigma = 2M$, $r_{hp} = 6M$ and $A = 8$. It is clear from the fig. 4.6 that introducing magnetic energy produces a clearer overall image, revealing more of the gas. The light curves for the case $\varepsilon = 0.5$ and $\varepsilon = 1$ are almost identical, with the only noticeable difference being the relative luminosity of the hotspot in comparison to other regions, which appears to be slightly higher in the latter case for certain snapshots (as depicted here). The case $\varepsilon = 0$ differs from the other but retains the same overall shape, differing only in amplitude. The main difference with the standard case is due to the hotspot and not the distribution function. Considering all factors, we opt for $\varepsilon = 0.5$ in this case, as it yields a brighter object. Overall, a robust magnetic contribution is imperative for generating the plasmoid.

Final Result

The final simulation parameters are as follows: $A = 8$, $\sigma = 2M$, $r_{hp} = 6M$ and $\varepsilon = 1$. In fig. 4.7, we present the most optimal scenario achieved using this simplified toy model. For completeness, we also include the co-rotating case, keeping the same parameter values. We did not delve deeper into the co-rotating case, as it has been extensively studied in previous studies (see GRAVITY Collaboration, Bauböck, M., et al. 2020 M. Wielgus et al. 2022). However, the comparison remains valid since a plasmoid generated by perturbation should ideally conserve the orbital angular momentum of the surrounding gas. Within the same figure, we depict a snapshot featuring two hotspots—one on the top left side and another on the top right side relative to the black hole. This is a useful comparison to the observation, although the latter is a time averaged image.

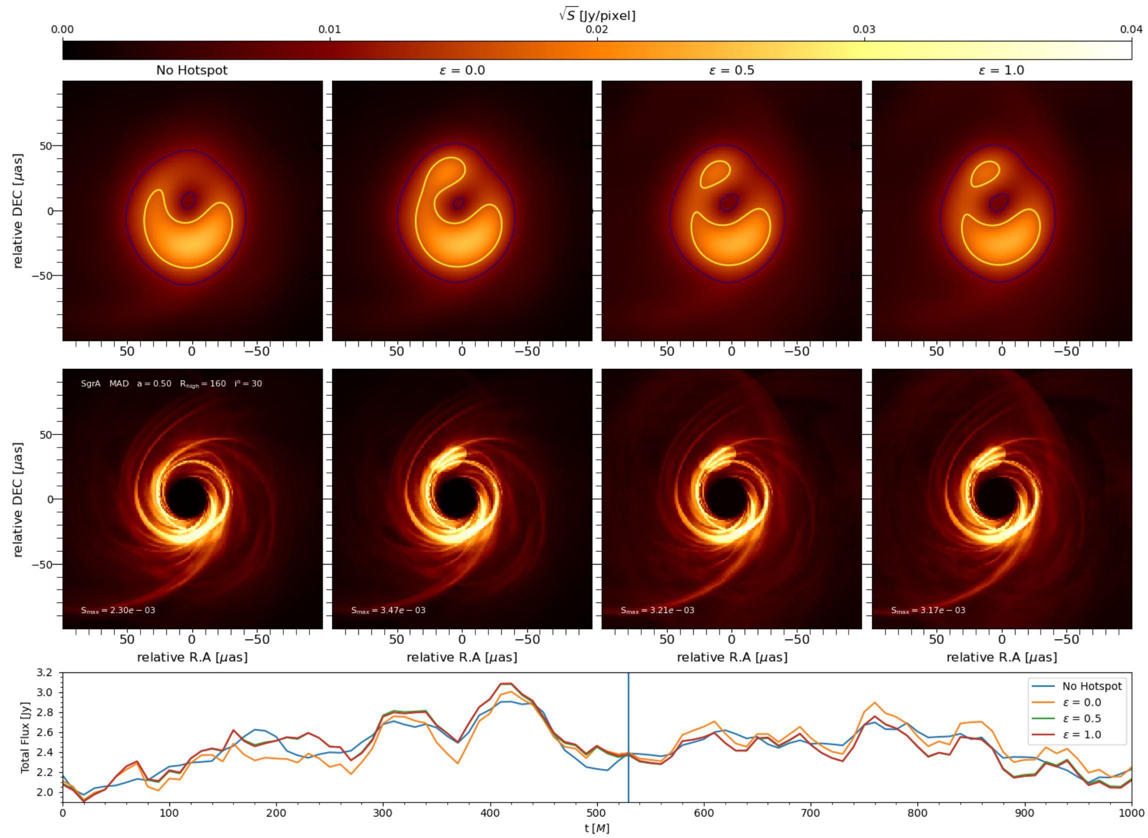

Figure 4.6: Impact of magnetic fraction using the Kappa distribution function. From left to right, the case thermal with no hotspot, then $\varepsilon = 0.0$,$\varepsilon = 0.5$,$\varepsilon = 1.0$. Each case is represented the direct image and the blurred one, simulating trivially the resolution of the telescope. The hotspot is situated on the top side of each image. On the bottom, it is shown the light curve for each case.

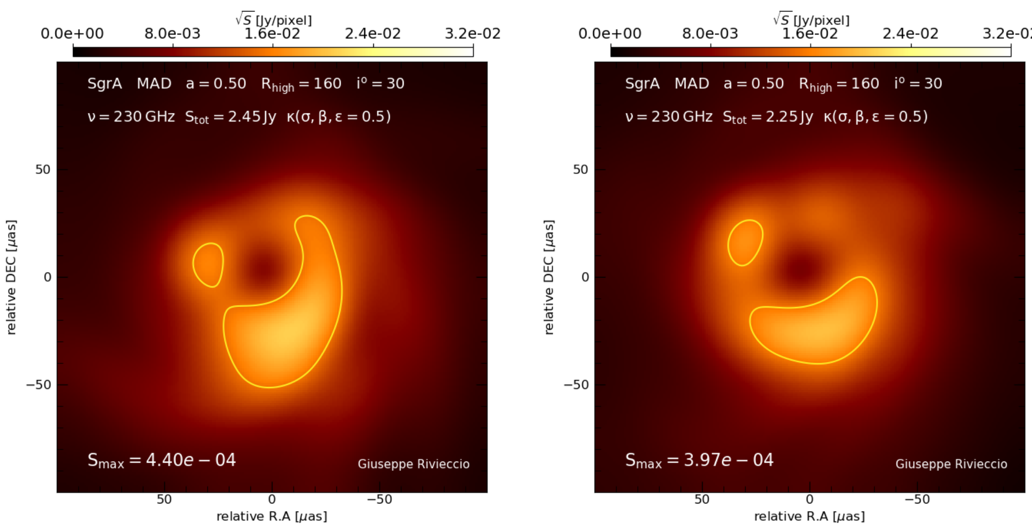

Figure 4.7: On the left, we have the counter-rotating case that we have been analyzing thus far. On the right, we observe the co-rotating case. These represent distinct snapshots respectively at $t_{counter} = 250M$ and $t_{co} = 110M$. Contour lines are utilized to identify the plasmoid located in the top left in both images. These contour lines delineate regions with emissions exceeding $1.55 \times 10^{-2} Jy/_{pixel}$.

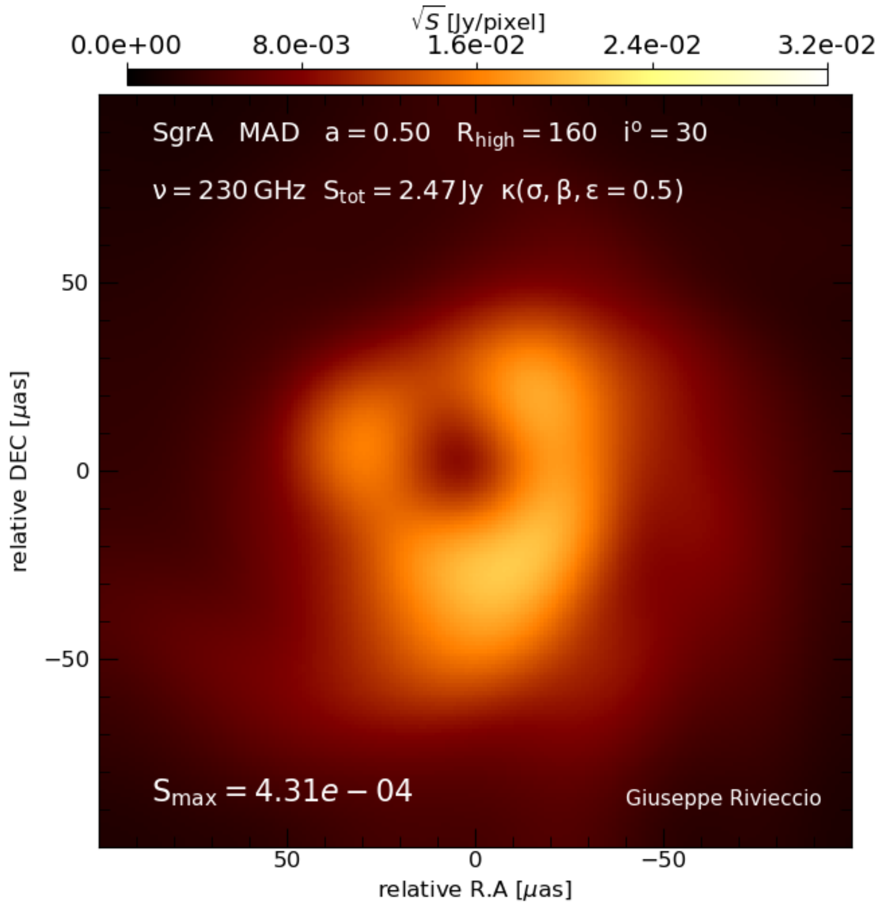

Figure 4.8: The simulation shows two hotspots, 60^o apart, one on the top left and one on the top right of the image.

–5–
Conclusions

Sgr A*, the supermassive black hole at the center of our Milky Way galaxy, has been a subject of intense study in recent decades. Despite the progress made, there remain intriguing mysteries waiting to be unraveled. Flare phenomena originating from this enigmatic celestial object have been widely observed, yet a definitive explanation has remained elusive.

One plausible hypothesis, which we delve into here, posits the existence of a hotspot in orbit around the black hole—a hotspot commonly believed to be a plasmoid generated through the process of magnetic reconnection. In this study, we investigate the potential impact of this object on the emission from Sgr A*, and to facilitate this exploration, we have developed a model that introduces modifications to the absorption and emission coefficients. Given that the genesis of the plasmoid is intimately connected with the magnetic field, it becomes imperative to incorporate magnetic effects into the emission model. In a broader sense, our model assumes the accretion disk to be magnetically dominated (MAD), indicating that the behavior of matter within it is significantly influenced by magnetic fields. To faithfully represent the magnetic contribution to the emission process, we leverage the kappa electron distribution function. Conversely, we compare this distribution with a relativistic thermal distribution (Maxwell-Juttner), wherein the magnetic component is solely associated with synchrotron emission and does not exert influence over the behavior of electrons.

Our results reveal that non-thermal particles have a substantial impact on the overall flux, although their influence on the plasmoid itself is less pronounced. In cases with a negligible magnetic contribution, the plasmoid becomes more distinguishable, mainly due to the kappa distribution yielding a flatter intensity profile. However, the ultimate model must align with the physical constraints and demands, suggesting that the optimal scenario involves a partial magnetic influence.

Furthermore, we have conducted an analysis of specific hotspot properties, including its size, distance from the black hole, and the amplitude of its effect within the hotspot. Our results suggest that an ideal hotspot scenario comprises a diameter of $4M$, positioned at a distance of $6M$ from the black hole. This finding indicates that the emission is significantly influenced by the jet base region, as indicated by our simulations. Additionally, the amplitude of the effect within the hotspot is approximately eight times greater than the background emission, suggesting that the gas within the hotspot possesses considerably higher energy levels than its surroundings, lending support to the plasmoid hypothesis.

It is essential to clarify that our aim is not to definitively establish the presence of a plasmoid in a stable circular orbit. Instead, we propose that the observed effects may be more accurately explained by a continuous production of plasmoids, giving rise to the observed flares. This concept is supported by previous research, such as Nathanail et al. 2020, which demonstrates the possibility of generating and ejecting plasmoids continuously. The hotspot model remains an area ripe for further investigation and discovery, offering a plausible explanation for the observed phenomena. In this study, we explore a simplified model to gain initial insights, recognizing that it provides a valuable approximation to assess the feasibility of the hotspot concept and justify the allocation of resources for more advanced and resource-intensive General Relativistic Magnetohydrodynamics (GRMHD) simulations.

Limits

With regard to the model employed in this study, a key consideration is that we did not analyze the time-averaged image derived from our simulations. This decision was based on the understanding that the hotspot contributes most significantly to a region where the flux is already consistent. Consequently, averaging over multiple revolutions would result in a brighter region at the bottom of the image without any discernible hotspot. A future improvement could involve modeling an ejection process to better replicate time-averaged observations.

Another limitation of this study is that we exsplored only one model: a spherical plasmoid with a Gaussian profile in a circular Keplerian orbit. Moreover, both the absorption and the emission coefficients were uniformly affected by model the parameters. To solve addres this limitation, we implemented also a Lorentzian profile, an independend variation of the coefficient, a rotating ellissoidal plasmoid and a quasi-circular orbit on the equatorial plane. However, all these implementation seemed to have minimal impact on the results and were subsequently discarded due to the computational complexity involved. We focused our efforts on the primary parameters that exhibited the most significant contributions.

Lastly, but by no means less important, it is worth noting that we did not have access to official observational data from the Event Horizon Telescope. All of our analyses had to be carried out qualitatively, lacking objective testing to confirm our hypotheses.

Bibliography

Goodwin, S. P., J. Gribbin, and M. A. Hendry (Aug. 1998). “The relative size of the Milky Way”. In: *The Observatory* 118, pp. 201–208.

Kafle, Prajwal R., Sanjib Sharma, Geraint F. Lewis, and Joss Bland-Hawthorn (Nov. 2012). “KINEMATICS OF THE STELLAR HALO AND THE MASS DISTRIBUTION OF THE MILKY WAY USING BLUE HORIZONTAL BRANCH STARS”. In: *The Astrophysical Journal* 761.2, p. 98. DOI: 10.1088/0004-637x/761/2/98. URL: https://doi.org/10.1088%2F0004-637x%2F761%2F2%2F98.

Genzel, R., D. Hollenbach, and C. H. Townes (May 1994). “The nucleus of our Galaxy”. In: *Reports on Progress in Physics* 57.5, pp. 417–479. DOI: 10.1088/0034-4885/57/5/001.

Ghez, A. M. et al. (Mar. 2003). “The First Measurement of Spectral Lines in a Short-Period Star Bound to the Galaxy’s Central Black Hole: A Paradox of Youth”. In: *The Astrophysical Journal* 586.2, p. L127. DOI: 10.1086/374804. URL: https://dx.doi.org/10.1086/374804.

GRAVITY Collaboration, Abuter, R., et al. (2023). “Polarimetry and astrometry of NIR flares as event horizon scale, dynamical probes for the mass of Sgr A*”. In: *A&A* 677, p. L10. DOI: 10.1051/0004-6361/202347416. URL: https://doi.org/10.1051/0004-6361/202347416.

EHT (2022a). “First Sagittarius A* Event Horizon Telescope Results. I. The Shadow of the Supermassive Black Hole in the Center of the Milky Way”. In: *The Astrophysical Journal Letters* 930.L12. URL: https://doi.org/10.3847/2041-8213/ac6674.

EHT et al. (Apr. 2019). “First M87 Event Horizon Telescope Results. I. The Shadow of the Supermassive Black Hole”. In: *The Astrophysical Journal Letters* 875.1, p. L1. DOI: 10.3847/2041-8213/ab0ec7. URL: https://dx.doi.org/10.3847/2041-8213/ab0ec7.

Luminet, J. -P. (May 1979). “Image of a spherical black hole with thin accretion disk.” In: 75, pp. 228–235.

EHT (2022b). “First Sagittarius A* Event Horizon Telescope Results. V. Testing Astrophysical Models of the Galactic Center Black Hole”. In: *The Astrophysical Journal Letters* 930.L16. URL: https://doi.org/10.3847/2041-8213/ac6672.

Brown, R. L. and K. Y. Lo (Feb. 1982). "Variability of the compact radio source at the Galactic Center." In: 253, pp. 108–114. DOI: 10.1086/159615.

Falcke, Heino et al. (May 1998). "The Simultaneous Spectrum of Sagittarius A* from 20 Centimeters to 1 Millimeter and the Nature of the Millimeter Excess". In: 499.2, pp. 731–734. DOI: 10.1086/305687. arXiv: astro-ph/9801085 [astro-ph].

An, T. et al. (Nov. 2005). "Simultaneous Multiwavelength Observations of Sagittarius A∗". In: *The Astrophysical Journal* 634.1, pp. L49–L52. DOI: 10.1086/498687. URL: https://doi.org/10.1086%2F498687.

Eckart, A. et al. (May 2006). "The flare activity of Sagittarius A* New coordinated mm to X-ray observations". English (US). In: *Astronomy and Astrophysics* 450.2, pp. 535–555. ISSN: 0004-6361. DOI: 10.1051/0004-6361:20054418.

Baganoff, F. K. et al. (July 2003). "Chandra X-Ray Spectroscopic Imaging of Sagittarius A* and the Central Parsec of the Galaxy". In: *The Astrophysical Journal* 591.2, p. 891. DOI: 10.1086/375145. URL: https://dx.doi.org/10.1086/375145.

Boyce, H. et al. (Jan. 2019). "Simultaneous X-Ray and Infrared Observations of Sagittarius A*'s Variability". In: *The Astrophysical Journal* 871.2, p. 161. DOI: 10.3847/1538-4357/aaf71f. URL: https://dx.doi.org/10.3847/1538-4357/aaf71f.

Wielgus, Maciek et al. (2022). "Millimeter Light Curves of Sagittarius A* Observed during the 2017 Event Horizon Telescope Campaign". In: *The Astrophysical Journal Letters* 930.L19, pp. 1–32. URL: https://doi.org/10.3847/2041-8213/ac6428.

Chen, Zhuo et al. (Sept. 2019). "Consistency of the Infrared Variability of SGR A$*over22yr$". In: *The Astrophysical Journal* 882.2, p. L28. DOI: 10.3847/2041-8213/ab3c68. URL: https://doi.org/10.3847%2F2041-8213%2Fab3c68.

Marrone, D. P. et al. (July 2008). "An X-Ray, Infrared, and Submillimeter Flare of Sagittarius A*". In: 682.1, pp. 373–383. DOI: 10.1086/588806. arXiv: 0712.2877 [astro-ph].

Dodds-Eden, K. et al. (May 2009). "EVIDENCE FOR X-RAY SYNCHROTRON EMISSION FROM SIMULTANEOUS MID-INFRARED TO X-RAY OBSERVATIONS OF A STRONG Sgr A* FLARE". In: *The Astrophysical Journal* 698.1, p. 676. DOI: 10.1088/0004-637X/698/1/676. URL: https://dx.doi.org/10.1088/0004-637X/698/1/676.

Ponti, G. et al. (Mar. 2017). "A powerful flare from Sgr A$*confirmsthesynchrotronnatureoftheX-rayemission$". In: *Monthly Notices of the Royal Astronomical Society* 468.2, pp. 2447–2468. DOI: 10.1093/mnras/stx596. URL: https://doi.org/10.1093%2Fmnras%2Fstx596.

Yuan, Feng, Eliot Quataert, and Ramesh Narayan (May 2004). "On the Nature of the Variable Infrared Emission from Sagittarius A∗". In: *The Astrophysical Journal* 606.2, pp. 894–899. DOI: 10.1086/383117. URL: https://doi.org/10.1086%2F383117.

Yusef-Zadeh, F. et al. (June 2006). "A Multiwavelength Study of Sgr A$*: TheRoleofNear-IRFlaresinProductionofX-Ray, Soft\gamma$-Ray, and Submillimeter Emission". In: *The*

Astrophysical Journal 644.1, pp. 198–213. DOI: 10.1086/503287. URL: https://doi.org/10.1086%2F503287.

Aimar, N. et al. (Mar. 2023). “Magnetic reconnection plasmoid model for Sagittarius A$*flares$”. In: *Astronomy &amp Astrophysics* 672, A62. DOI: 10.1051/0004-6361/202244936. URL: https://doi.org/10.1051%2F0004-6361%2F202244936.

Bostick, Winston H. (1957). “EXPERIMENTAL STUDY OF PLASMOIDS”. In: *Physical Review* 107, pp. 1736–1736. URL: https://api.semanticscholar.org/CorpusID:123393057.

Broderick, Avery E. and Abraham Loeb (Oct. 2005). “Imaging bright-spots in the accretion flow near the black hole horizon of Sgr A*”. In: *Monthly Notices of the Royal Astronomical Society* 363.2, pp. 353–362. ISSN: 0035-8711. DOI: 10.1111/j.1365-2966.2005.09458.x. eprint: https://academic.oup.com/mnras/article-pdf/363/2/353/3903626/363-2-353.pdf. URL: https://doi.org/10.1111/j.1365-2966.2005.09458.x.

Wielgus, M. et al. (Sept. 2022). “Orbital motion near Sagittarius Asup$*/sup$”. In: *Astronomy &amp Astrophysics* 665, p. L6. DOI: 10.1051/0004-6361/202244493. URL: https://doi.org/10.1051%2F0004-6361%2F202244493.

Jackson, John David (1998). *Classical Electrodynamics, 3rd Edition*.

GRAVITY Collaboration, Bauböck, M., et al. (2020). “Modeling the orbital motion of Sgr A*´s near-infrared flares”. In: *A&A* 635, A143. DOI: 10.1051/0004-6361/201937233. URL: https://doi.org/10.1051/0004-6361/201937233.

Chandrasekhar, S. (1992). *The Mathematical Theory of Black Holes*. International series of monographs on physics. Oxford University Press. ISBN: 9780198520504. URL: https://books.google.es/books?id=LBaRwAACAAJ.

O’Neill, Barrett (1995). *The geometry of Kerr black holes*.

Rezzolla, Luciano and Olindo Zanotti (Sept. 2013). *Relativistic Hydrodynamics*. Oxford University Press. ISBN: 9780198528906. DOI: 10.1093/acprof:oso/9780198528906.001.0001. URL: https://doi.org/10.1093/acprof:oso/9780198528906.001.0001.

Abramowicz, Marek A. and P. Chris Fragile (Jan. 2013). “Foundations of Black Hole Accretion Disk Theory”. In: *Living Reviews in Relativity* 16.1. DOI: 10.12942/lrr-2013-1. URL: https://doi.org/10.12942%2Flrr-2013-1.

Lazar, Marian and Horst Fichtner (2021). “Kappa Distribution Function: From Empirical to Physical Concepts”. In: *Kappa Distributions: From Observational Evidences via Controversial Predictions to a Consistent Theory of Nonequilibrium Plasmas*. Ed. by Marian Lazar and Horst Fichtner. Cham: Springer International Publishing, pp. 107–123. ISBN: 978-3-030-82623-9. DOI: 10.1007/978-3-030-82623-9_6. URL: https://doi.org/10.1007/978-3-030-82623-9_6.

Livadiotis, G. and D. J. McComas (2009). “Beyond kappa distributions: Exploiting Tsallis statistical mechanics in space plasmas”. In: *Journal of Geophysical Research: Space Physics* 114.A11. DOI: `https://doi.org/10.1029/2009JA014352`. eprint: `https://agupubs.onlinelibrary.wiley.com/doi/pdf/10.1029/2009JA014352`. URL: `https://agupubs.onlinelibrary.wiley.com/doi/abs/10.1029/2009JA014352`.

Einstein, Albert (Jan. 1915). “Die Feldgleichungen der Gravitation”. In: *Sitzungsberichte der Königlich Preussischen Akademie der Wissenschaften*, pp. 844–847.

Misner, C.W., K.S. Thorne, and J.A. Wheeler (1973). *Gravitation*. Gravitation pt. 3. W. H. Freeman. ISBN: 9780716703440. URL: `https://books.google.it/books?id=w4Gigq3tY1kC`.

Carroll, Sean M. (2019). *Spacetime and Geometry: An Introduction to General Relativity*. Cambridge University Press. DOI: `10.1017/9781108770385`.

Schwarzschild, K. (Jan. 1916). “On the Gravitational Field of a Mass Point According to Einstein’s Theory”. In: *Abh. Konigl. Preuss. Akad. Wissenschaften Jahre 1906,92, Berlin,1907* 1916, pp. 189–196.

Weizsäcker, Carl Friedrich (Nov. 1948). “Die Rotation kosmischer Gasmassen”. In: *Zeitschrift Naturforschung Teil A* 3, pp. 524–539. DOI: `10.1515/zna-1948-8-1118`.

Balbus, Steven A. and John F. Hawley (July 1991). “A Powerful Local Shear Instability in Weakly Magnetized Disks. I. Linear Analysis”. In: 376, p. 214. DOI: `10.1086/170270`.

Narayan, Ramesh, Igor V. Igumenshchev, and Marek A. Abramowicz (Dec. 2003). “Magnetically Arrested Disk: an Energetically Efficient Accretion Flow: Fig. 1”. In: *Publications of the Astronomical Society of Japan* 55.6, pp. L69–L72. DOI: `10.1093/pasj/55.6.l69`. URL: `https://doi.org/10.1093%2Fpasj%2F55.6.l69`.

Blandford, R. D. and R. L. Znajek (May 1977). “Electromagnetic extraction of energy from Kerr black holes.” In: 179, pp. 433–456. DOI: `10.1093/mnras/179.3.433`.

Younsi, Z., K. Wu, and S. V. Fuerst (Aug. 2012). “General relativistic radiative transfer: formulation and emission from structured tori around black holes”. In: *&amp Astrophysics* 545, A13. DOI: `10.1051/0004-6361/201219599`. URL: `https://doi.org/10.1051%5C%2F0004-6361%5C%2F201219599`.

Vasyliunas, Vytenis M. (May 1968). “A survey of low-energy electrons in the evening sector of the magnetosphere with OGO 1 and OGO 3”. In: 73.9, pp. 2839–2884. DOI: `10.1029/JA073i009p02839`.

Pierrard, V. and M. Lazar (Nov. 2010). “Kappa Distributions: Theory and Applications in Space Plasmas”. In: 267.1, pp. 153–174. DOI: `10.1007/s11207-010-9640-2`. arXiv: `1003.3532 [physics.space-ph]`.

Eyelade, Adetayo V., Marina Stepanova, Cristóbal M. Espinoza, and Pablo S. Moya (Mar. 2021). “On the Relation between Kappa Distribution Functions and the Plasma Beta Parameter in the Earth’s Magnetosphere: THEMIS Observations”. In: *The Astrophysical*

Journal Supplement Series 253.2, p. 34. DOI: 10.3847/1538-4365/abdec9. URL: https://dx.doi.org/10.3847/1538-4365/abdec9.

Fromm, Christian M. et al. (Apr. 2022). "Impact of non-thermal particles on the spectral and structural properties of M87". In: *Astronomy &amp Astrophysics* 660, A107. DOI: 10.1051/0004-6361/202142295. URL: https://doi.org/10.1051%5C%2F0004-6361%5C%2F202142295.

Moscibrodzka, Monika A., Heino Falcke, and Hotaka Shiokawa (2015). "General relativistic magnetohydrodynamical simulations of the jet in M 87". In: *Astronomy and Astrophysics* 586, pp. 1–15.

Gary, G. Allen (Oct. 2001). "Plasma Beta above a Solar Active Region: Rethinking the Paradigm". In: 203.1, pp. 71–86. DOI: 10.1023/A:1012722021820.

Pandya, Alex, Zhaowei Zhang, Mani Chandra, and Charles F. Gammie (May 2016). "POLARIZED SYNCHROTRON EMISSIVITIES AND ABSORPTIVITIES FOR RELATIVISTIC THERMAL, POWER-LAW, AND KAPPA DISTRIBUTION FUNCTIONS". In: *The Astrophysical Journal* 822.1, p. 34. DOI: 10.3847/0004-637X/822/1/34. URL: https://dx.doi.org/10.3847/0004-637X/822/1/34.

Leung, Po Kin, Charles F. Gammie, and Scott C. Noble (July 2011). "NUMERICAL CALCULATION OF MAGNETOBREMSSTRAHLUNG EMISSION AND ABSORPTION COEFFICIENTS". In: *The Astrophysical Journal* 737.1, p. 21. DOI: 10.1088/0004-637X/737/1/21. URL: https://dx.doi.org/10.1088/0004-637X/737/1/21.

Nathanail, Antonios et al. (May 2020). "Plasmoid formation in global GRMHD simulations and AGN flares". In: *Monthly Notices of the Royal Astronomical Society* 495.2, pp. 1549–1565. ISSN: 0035-8711. DOI: 10.1093/mnras/staa1165. eprint: https://academic.oup.com/mnras/article-pdf/495/2/1549/33301461/staa1165.pdf. URL: https://doi.org/10.1093/mnras/staa1165.